Journal of Photochemistry & Photobiology, B: Biology 274 (2026) 113319

Contents lists available at ScienceDirect

Journal of Photochemistry & Photobiology, B: Biology

journal homepage: www.elsevier.com/locate/jphotobiol

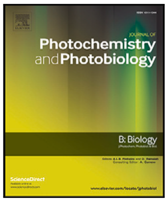

Scalable fabrication of polymeric dissolving microneedles for optimized ALA delivery in photodynamic therapy

Dianeth Sara Lima Bejar [a], Michelle Barreto Requena [a,b,*], Mirian Denise Stringasci [a], Marlon Rodrigues Garcia [c], Erika Toneth Ponce Ayala [a], Juliana Cristina Barreiro [a], Sebastião Pratavieira [a], Vanderlei Salvador Bagnato [a,b]

[a] *São Carlos Institute of Physics, University of São Paulo, São Carlos, 13566590, Brazil*
[b] *Department of Biomedical Engineering, Texas A&M University, CPRIT Scholar in Cancer Research, College Station, 77843, TX, USA*
[c] *School of Engineering, Sao Paulo State University, São João da Boa Vista, 13566590, São Paulo, Brazil*

ARTICLE INFO

Keywords:
Photodynamic therapy
Dissolving microneedles
ALA
Gantrez AN-139
Skin cancer
Drug delivery

ABSTRACT

Topical photodynamic therapy (PDT) is a minimally invasive, clinically approved treatment for non-melanoma skin cancer that relies on the conversion of photosensitizer (PS) precursors such as 5-aminolevulinic acid (ALA) into protoporphyrin IX (PpIX), followed by light activation. However, the low skin penetration of topically applied ALA cream remains a major limitation, restricting effective PpIX accumulation in deeper tumor layers. To address this challenge, we produced dissolving microneedles (DMN) as an alternative intradermal delivery platform. Two mold types were evaluated for DMN fabrication, one with a slight edge (DMNe) and another without edges (DMNf), both maintaining a conical tip geometry. DMN were prepared with a formulation containing initially 10% ALA and 20% Gantrez® AN-139 polymer in water, produced in a few steps, and characterized. *In vitro* insertion studies demonstrated consistent penetration depths of approximately 250 μm with minimal tip deformation. DMNf showed a better penetration efficiency than the DMNe and cream groups, and mass spectrometry confirmed uniform ALA distribution. *In vitro* assays in darkness confirmed the formulation's biocompatibility with tumor cells. In a murine xenograft model of nodular epidermoid carcinoma, DMN-mediated ALA delivery generated up to twice the amount of PpIX in deeper tumor regions and also caused greater PDT damage compared to cream application. These findings highlight DMN as a promising approach to enhance PDT efficacy, especially for thicker or nodular skin lesions, by enabling superior and uniform intradermal drug delivery.

1. Introduction

Non-melanoma skin cancer (NMSC) is a prevalent malignant neoplasm characterized by uncontrolled cellular proliferation in the epidermis [1]. Although associated with low mortality, NMSC represents the most common cancer worldwide, with incidence rates surpassing those of all other malignancies combined. The two main subtypes are basal cell carcinoma (BCC) and squamous cell carcinoma (SCC) [2–4].

BCC is the most common subtype of skin cancer. It originates from the mutation of basal cells, which in healthy tissue form a single layer at the base of the epidermis and undergo continuous proliferation and differentiation. These mutations, driven primarily by long-term UV exposure along with factors like age and genetic predisposition, lead to uncontrolled proliferation and subsequent tumor formation [2]. Although BCC has the lowest mortality rate, it can cause substantial deformities and significantly impact quality of life, particularly in patients with comorbidities [5]. From both clinical and histopathological perspectives, BCC is predominantly classified into three major subtypes: superficial, nodular, and infiltrative (including morpheaform and sclerosing variants)(Fig. 1a). Clinical management is customized according to the tumor subtype, size, anatomical location, depth of invasion, and individual factors of the patient [6,7]. The standard treatment for BCC is surgical excision, which may be combined with radiation therapy [7,8], chemotherapy, cryotherapy, immunotherapy, and Mohs micrographic surgery for high-risk BCC [9]. However, these conventional techniques require specialized infrastructure and personnel, which may not be widely available. As a result, patients in many regions, particularly in less developed countries, face long waiting times that can worsen their conditions [10]. In this context, topical PDT stands out as a promising alternative.

---

* Corresponding author.
E-mail address: requenamichelle@tamu.edu (M.B. Requena).

https://doi.org/10.1016/j.jphotobiol.2025.113319
Received 13 October 2025; Received in revised form 20 November 2025; Accepted 26 November 2025

Topical PDT is an outpatient technique that requires minimal infrastructure investment, making it more economically accessible [5,11]. It is a patient-friendly option with a few side effects, excellent aesthetic outcomes, and high patient acceptance. PDT can also be a viable option for unsuitable patients for surgery [10]. The treatment relies on a photosensitizer (PS), a light source with a specific wavelength, and molecular oxygen in the targeted tissue. Their interaction generates reactive oxygen species (ROS), which induce the death of tumor cells [12]. Currently, the clinical PDT protocol for skin cancer relies on the topical application of protoporphyrin IX (PpIX) precursors. The PpIX precursors approved by the regulatory agencies of the United States (Food and Drug Administration, FDA) and Europe (European Medicines Agency, EMA) for clinical use in the treatment of certain precancerous lesions, such as actinic keratosis, as well as non-melanoma skin cancers, are 5-aminolevulinic acid (ALA, Levulan®) and its methyl ester derivative, methyl aminolevulinate (MAL, Metvix®) [13–18].

In Brazil, numerous fundamental and clinical studies on topical PDT for the treatment of superficial BCC have been conducted. In our research group, the clinical trials for non-melanoma skin cancer demonstrated high cure rates, with more than 95% cure rate for tumors of 2 mm thickness and around 85% for tumors up to 9 mm [5,19]. Currently, the treatment, prodrugs, and light irradiation devices are incorporated into the Brazilian public healthcare system. However, the approved clinical protocols for topical ALA or MAL-PDT are limited to superficial lesions, due to the limited skin penetration of the light and the cream (Fig. 1b). ALA also presents important limitations related to its physicochemical characteristics. Its pronounced hydrophilicity and zwitterionic nature reduce membrane permeability, which in turn restricts its ability to penetrate intradermal tissues [20]. To overcome these limitations, various intradermal drug delivery strategies have been investigated to enhance skin permeation and drug penetration, including sonophoresis [21], iontophoresis [22], and microneedling technology [23,24].

Microneedles (MNs) have gained significant attention as an intradermal PS delivery method in recent years [25–29]. MNs can penetrate the skin's protective barrier by creating microchannels during insertion, facilitating drug permeation and enabling delivery to the intradermal layers (Fig. 1c). Their shallow insertion depth typically minimizes pain and bleeding [30,31]. Different materials and designs have been employed in the MNs fabrication, including silicon, stainless steel, and biodegradable polymers. Metallic and silicon MNs provide rigidity and mechanical strength [23], enhancing topical drug permeability through a two-step procedure. The first MNs developed for PDT were developed with these solid MNs through complex processes and coated with ALA or PS. However, these materials may present biocompatibility issues, potentially causing adverse skin reactions [32]. In contrast, dissolving microneedles (DMNs), composed of biocompatible polymers, penetrate the skin and gradually release drugs into the intradermal layers, thereby minimizing skin reactions. Among the most commonly employed polymers are polylactic acid (PLA) [33], polyvinylpyrrolidone (PVP) [34], poly(lactic-co-glycolic acid) (PLGA) [35], polyglycolic acid (PGA) [36], carboxymethyl cellulose (CMC) [37], hyaluronic acid (HA) [26–28,38] and methyl vinyl ether/maleic anhydride copolymers (PVM/MA) [24,39]. These materials are selected based on their mechanical strength, solubility, biocompatibility, and degradation kinetics, which collectively allow precise control over the PS release profile. For ALA application, the use of DMN would enhance drug penetration into deeper tumor layers. This improved delivery would increase the precursor availability to a greater number of cells, thereby potentiating the production of PpIX more rapidly compared to the current standard cream application used in clinical practice, which effectively is reduced for nodular BCC compared to superficial [40].

Donnelly et al. (2008) proposed for the first time a model of silicon MN coated with ALA and compared it with adhesive biopatches tested and validated previously [23,41]. Recent studies have demonstrated the potential of DMNs in PS delivery within tumor tissue, particularly with formulations combining ALA and hyaluronic acid, which have shown superior PpIX production compared to topical application in an oral epidermoid carcinoma (KB) tumor and in rat skin models [38,42] and higher tumor inhibition rates compared to injection delivery [26]. Zhao et al. (2018) developed a model of tip-loaded DMNs made of hyaluronic acid, delivering 0.61 mg ALA and achieving 97% tumor inhibition in a subcutaneous model. Zhu et al. (2019) related the development of a stable hyaluronic acid DMN loaded with ALA for PDT. This system enhanced skin delivery and demonstrated superior efficacy in eradicating superficial tumors *in vivo* compared to injectable ALA solution, with stability maintained for up to 9 months. Gang H. et al. (2022) have explored the use of hyaluronic acid-based DMNs loaded with nanoparticles with ALA and catalase encapsulated. These strategies are designed to enhance intratumoral drug delivery, with the dual goals of boosting PpIX accumulation and inhibiting the enzyme ferrochelatase, which is responsible for iron incorporation into PpIX to complete heme biosynthesis. By preventing this conversion, the approach seeks to maximize PpIX levels, subsequently increase ROS generation upon irradiation, and ultimately improve PDT efficacy [43]. However, the complexity of these formulations, alongside the challenges in their clinical translation and manufacturing scalability, makes their adoption by public healthcare systems a distant prospect.

Other researchers have investigated the fabrication and application of MN based on Gantrez AN-139, a copolymer of methyl vinyl ether and maleic anhydride (PVM/MA). This polymer is characterized by its biodegradability, high biocompatibility, and bioadhesive properties. It is listed in the U.S. Food and Drug Administration (FDA) database for topical applications and dental products [44–46]. Donnelly et al. (2005) developed bioadhesive patches for ALA delivery using Gantrez AN-139. These formulations demonstrated promising stability and controlled release. Also, they reported that ALA patches for onychomycosis exhibited limited skin penetration, highlighting the importance of overcoming the penetration barrier for therapeutic efficacy [47]. In a subsequent 2014 study, the group developed both hydrogel-forming and dissolving MN via micromolding. While the needles, which featured 8-sided pyramid tips, exhibited some distortion in the tips' formation, they maintained their structural integrity and performed effectively in porcine skin models, with no significant differences observed between the two types [32]. In 2022, Requena et al. introduced a pyramidal DMN design containing 5% w/w ALA and Gantrez AN-139, fabricated with commercial molds for use in murine tumor models. PpIX production was assessed and compared with that achieved using a cream formulation. The use of DMNs in combination with local heating improved PpIX distribution in deeper tumor layers [24]. However, a 5% ALA dose may be insufficient to achieve a therapeutic effect in clinical studies on BCC, which the standard treatment involves 20% ALA [5].

This study introduces a key innovation by increasing the ALA concentration two-fold in the initial DMN formulation to enhance the transdermal delivery of ALA, employing a scalable and straightforward fabrication protocol based on the polymer Gantrez AN-139. Regarding DMNs molds, tips geometry are widely explored [48–52], whereas the formation of the wall at the base is scarcely discussed. To address this gap, we investigated two distinct conical DMN designs, evaluating the mold base formation for the first time while maintaining the proven conical tip shape [48], considering the differences between the production process and revealing critical differences in skin penetration and drug delivery performance. This comparative approach not only optimizes the potential of ALA-PDT but also provides novel insights into how DMN array geometry influences therapeutic outcomes. Our work combines *in vitro* characterization of these high-load DMN with a subdose of PDT and histological evaluation in a nodular murine tumor model, offering a strategic advancement toward more effective and targeted PDT protocols.

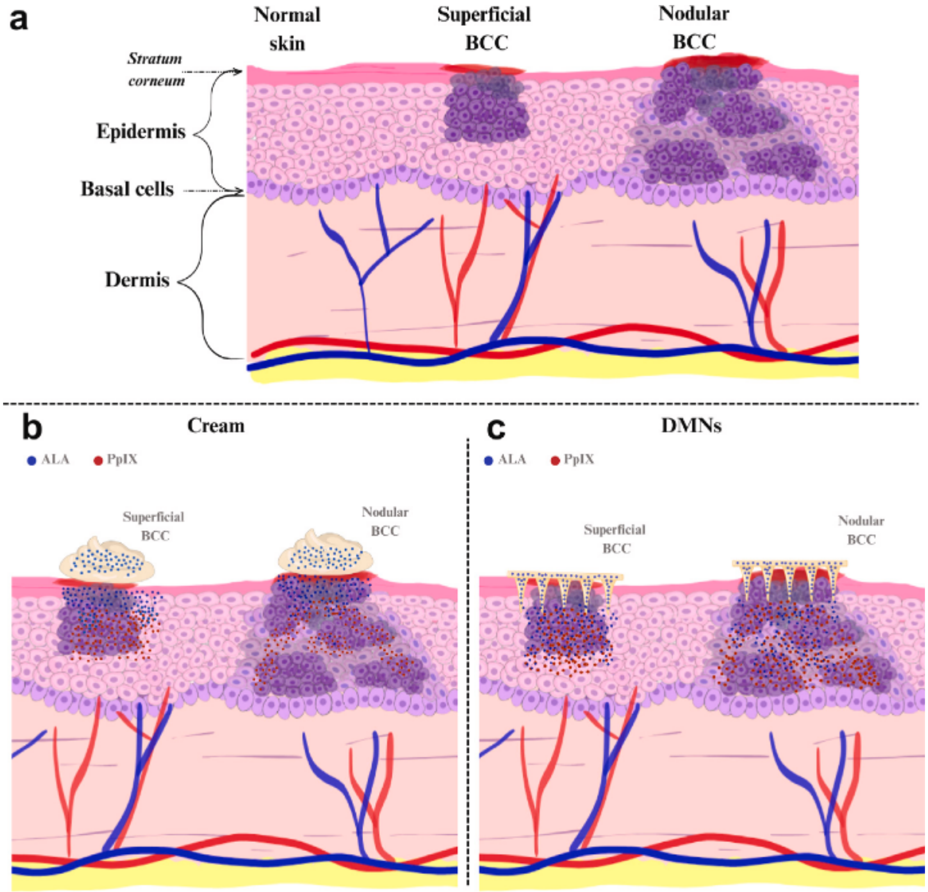

Fig. 1. (a) Representative images for comparison of the main BCC types with normal skin. Comparison of drug penetration and PpIX production (red dots) in superficial and nodular BCC according to the drug delivery strategy: (b) cream and (c) DMN application.

2. Materials and methods

2.1. Formulation

Hydrochloride 5-ALA was obtained as a powder from EmiPharma (Embrapii program, Brazil). Gantrez^{TM} AN-139 was gifted as a powder from Ashland (Wilmington, USA). A 30% w/w Gantrez stock formulation was prepared in Milli-Q water and maintained at 95–100 °C in a water bath within an incubator (SSDcr, SolidSteel®, Brazil). The Gantrez-ALA formulation containing 10% w/w ALA and 20% w/w Gantrez was prepared in Milli-Q water, mixed at room temperature, and subsequently centrifuged at 3500 rpm for 15 min to ensure homogenization [24]. The polymer concentration used in this work follows values described and recommended in the literature for polymeric materials such as hydrogels, as it provides the mechanical strength and stability required for microneedles [53,54]. For comparison, an oil-in-water emulsion cream with ethylenediaminetetraacetic acid (EDTA) 0.15% and ALA 10% w/w, formulation developed for clinical use, was obtained from EmiPharma (Embrapii program, Brazil) [55].

2.2. Fabrication and characterization of ALA-DMN patches

The master template was produced via 3D printing (Form 2, FormLabs, USA) and used to fabricate polydimethylsiloxane (PDMS) molds in collaboration with the National Laboratory of Nanotechnology (LNNano) at the National Center for Research in Energy and Materials (CNPEM - Process No. 20220606). Two molds with conical tips were designed based on geometries reported in the literature to achieve an optimal balance between effective skin penetration and controlled dissolution [48]. Key dimensions, including height, tip geometry, and inter-needle spacing, were determined through a comprehensive literature review to ensure effective skin penetration while minimizing pain and bleeding [48,49,52,56]. The first mold design incorporated a slight edge to demarcate the formulation deposition area, resulting in microneedles with defined edges (DMNe) (Fig. 2a and 2c). In contrast, the second mold did not have edges, producing flat DMNs (DMNf) (Fig. 2b and 2d). Both molds were designed with a 13 × 13 grid of cone-shaped holes, approximately 450–500 μm in length, 300 μm at the base, and 200–250 μm spacing (Fig. 2e).

For the preparation of the ALA-DMNe and ALA-DMNf patches, 140 mg of the Gantrez-ALA formulation (10% w/w ALA and 20% w/w Gantrez) was added to the corresponding mold and placed in a pressurized chamber (VCR Equipamentos, Brazil) to minimize bubble formation and ensure complete filling. Pressure was increased to 1.5 kgf/cm^2 for 5 min, and the cycle was repeated after gradual depressurization. The drying process was optimized to produce stable DMNs with maintained mechanical integrity. For this purpose, the filled molds were placed in a desiccator within a drying oven at 25 °C for 72 h. After drying, both ALA-DMN and Gantrez-DMN patches were removed from the molds, sealed, and stored in a refrigerator, protected from humidity and light. The morphology and array structure of the DMN tips were characterized by scanning electron microscopy (SEM).

2.3. In vitro experiments

2.3.1. DMN insertion capability

To simulate MN insertion into the skin, we used the Parafilm polymeric membrane model (Parafilm M®, Bemis Company, Inc., USA) together with a test method employing a Texture Analyzer System (Stable Micro Systems, Surrey, US). This methodology was characterized

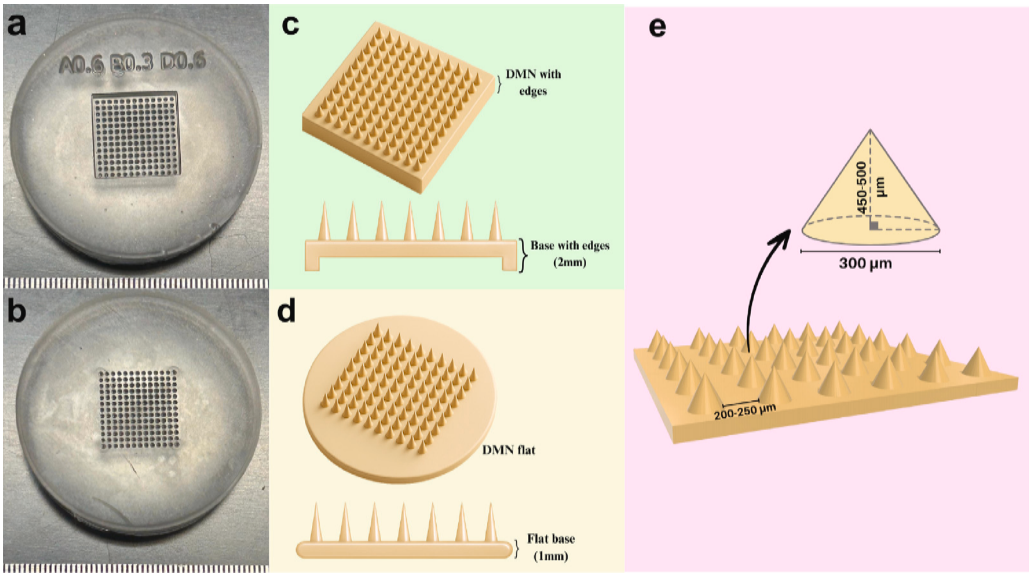

Fig. 2. (a) Mold with a slight edge designed to delimit formulation deposition. (b) Mold for the flat model without edge constraints. (c-d) Schematic representation and a cross-sectional view of the DMNs: (c) with slight edges (DMNe), and (d) the flat one (DMNf). (e) Schematic representation and dimensions of the conical tip array in both DMN.

and validated by Larrañeta et al. for *in vitro* insertion studies [57]. The experiment consisted of pressing the DMN array into nine stacked parafilm layers using the Texture Analyzer System with a force of 32 *N* for 30 s, replicating the pressure typically applied by a human finger during MN application [57,58]. The number of perforations per layer was determined using an optical stereomicroscope (Zeiss Stemi DV4, Carl Zeiss, Germany). The insertion efficiency was calculated as the percentage of holes formed at each depth, based on the thickness of the parafilm layers (125 μm) and the number of perforations observed.

2.3.2. MALDI-TOF mass spectrometry analysis

Thin circular films (3 mm diameter, 1 mm thickness approximately) were fabricated using 100 mg of formulation containing 10% of ALA (10 mg) and 20% of Gantrez (20 mg) diluted in water. These films were analyzed by matrix-assisted laser desorption/ionization time-of-flight (MALDI-TOF) mass spectrometry to evaluate possible chemical interactions between the polymer and ALA that could compromise its biological activity.

MALDI mass measurements were performed in positive-ion reflection mode using a Bruker AutoFlex-Max TOF/TOF instrument (Bruker, Bremen, Germany) equipped with a 355 nm, 2 kHz Nd:YAG laser. The mass spectra were processed by Flex Analysis software (Bruker Daltonics, Bremen, Germany), where external calibration was performed using MBT STAR-ACS (Bruker, Bremen, Germany), an antibiotic standard mixture. ALA sample solutions were mixed at a 1:1 (v/v) ratio with a 10 mg/mL HCCA solution (α-cyano-4-hydroxycinnamic acid, Bruker) to obtain final ALA concentrations of 5, 10, 25, 30, and 40 mg/mL, which were used to construct a calibration curve for determining the ALA concentration in the films. An acetaminophen solution (20 μg/mL) was employed as an internal standard, whose intensity peak was used to normalize the ALA signal [59].

Mass spectrometry imaging (MSI) was performed in positive-ion mode with a spatial resolution of 50 μm, accumulating 200 laser shots per pixel. The films were mounted on indium tin oxide (ITO)-coated glass slides to provide a conductive surface and marked for MALDI imaging. Imaging data were acquired and processed using FlexImaging 3.0 software (Bruker Daltonics). The method and parameters followed Requena et al. [59].

2.3.3. Cytotoxicity assessment in A-431 cells

Gantrez AN-139 is widely recognized as biocompatible and safe for use in drug delivery systems and cosmetic formulations. Nevertheless, a pilot assay was performed to verify the safety of the ALA-DMN patches. For this purpose, the epidermoid carcinoma cell line (ATCC®, A-431, CRL-1555) was used. Cells were cultured in Dulbecco's Modified Eagle's Medium (DMEM, Thermo Fisher Scientific, USA), supplemented with 10% (v/v) fetal bovine serum, and maintained at 37 °C in a humidified atmosphere containing 5% CO_2. A total of 2×10^4 cells were seeded into 96-well plates and cultured for 24 h. The circular films were dissolved in 1 mL of culture medium to prepare a stock solution. From this stock, final solutions were prepared at concentrations of 10, 5, 2.5, 1, and 0.1 mg/mL. Similarly, a Gantrez film was dissolved in 1 mL of culture medium, and final solutions were prepared at the same concentrations. Cells were incubated with the final solutions for 24 h. After medium removal, cell viability was assessed using the Alamar Blue assay (Thermo Fisher Scientific, USA) by adding one-tenth of the culture medium volume of the indicator. Following a 4-hour incubation, absorbance was measured at 570/600 nm using a Thermo Scientific Multiskan microplate reader (Waltham, USA).

2.4. In vivo experiments

2.4.1. Animal model and tumor induction

Forty-five female BALB/c athymic nude mice (6–9 weeks old, 25–30 g) were obtained from the Central Bioterium Facility of the Faculty of Medicine, University of São Paulo. The A-431 Squamous Cell Carcinoma (SCC) cell line was used to induce tumors characterized by a nodular and non-cystic morphology. This growth pattern, which contrasts with that of BCC models, providing a established model for this form of non-melanoma skin cancer [60,61]. Inoculation was performed by intradermal injection of 10^6 cells re-suspended in 50 μL phosphate-buffered saline (PBS) into the right flank of each animal. The experiments were conducted once tumors reached volumes between 15 and 25 mm^3. Tumor volume was estimated using the ellipsoidal formula $V = (\pi/6)abh$, where a and b correspond to perpendicular diameters and h to tumor thickness, measured with a vernier caliper. All procedures were approved by the Animal Use Ethics Committee of the São Carlos Institute of Physics, University of São Paulo (Protocol No. 3928020922).

2.4.2. PDT irradiation parameters and histological evaluation

PDT was performed using the LINCE® system (MMOptics, São Carlos, Brazil), equipped with a treatment probe emitting at 630 nm with an irradiation area of 9 cm^2. When tumors reached the target volume, intradermal PpIX delivery was achieved via ALA-DMNe, ALA-DMNf, or cream application, followed by a 60-minute incubation period, in accordance with previously reported protocols [62,63]. Subsequently, light irradiation was applied at an irradiance of 40 mW/cm^2 and a fluence of 30 J/cm^2, corresponding to a sub-therapeutic dose intended to induce photodynamic damage while avoiding complete tumor eradication [24,64]. Photodynamic damage in the tumor and overlying skin was assessed 72 h post-treatment by hematoxylin and eosin (H&E) histological analysis. Slides were scanned and digitized using a Grundium Ocus®20 scanner (Tampere, Finland) to enable comparative evaluation of tissue alterations. Each protocol was performed in quadruplicate. Throughout all procedures, animals were anesthetized with inhaled isoflurane (BioChimico®, Itatiaia, Rio de Janeiro, Brazil).

2.4.3. In vivo fluorescence measurements

To monitor PpIX generation and distribution in the superficial regions of the tumor and adjacent tissue during PDT, PpIX fluorescence was collected at three time points: (i) before DMNe, DMNf, or cream application (endogenous fluorescence), (ii) after a 60-minute incubation period, and (iii) after PDT [65]. Additionally, PpIX accumulation over time was evaluated in the tumor and adjacent tissue by PpIX fluorescence measurements collected before and after DMNf or cream application, at incubation times of 30, 60, and 120 min. PpIX fluorescence was collected using three methods: widefield fluorescence imaging in (i) visible range and (ii) near-infrared (NIR) range, and (iii) steady-state fluorescence spectroscopy (SSFS).

The first method, widefield visible fluorescence imaging, comprised the use of the fluorescence probe of the LINCE® system, coupled to an RGB digital camera (Canon EOS Rebel T7, Brazil) for fluorescence image acquisition in the red range. The fluorescence probe is an optical setup comprising a light-emitting diode (LED) with an excitation wavelength of 400 ± 10 nm, with a maximum output power of 50 ± 10 mW/cm^2 [66].

The second method, widefield NIR fluorescence imaging, was performed with a prototype designed to acquire near-infrared fluorescence images of PpIX, comprehensively described and characterized in previous works [62,67]. Briefly, the excitation system was composed of a diode laser emitting at 633 nm, coupled to an FD1-1646 optical fiber with a 600 μm core and a microlens for homogeneous irradiation. A 650 nm short-pass filter was used to suppress residual excitation light. Fluorescence was detected around 700 nm using a Thorlabs CMOS camera (model DCC-1545M, with ~46% efficiency at 700 ± 10 nm), through a band-pass filter with a full width at half maximum (FWHM) of 20 nm, centered at 700 nm, and an objective lens for image focusing [62]. Laser intensity and detection parameters of the camera were kept constant across all experiments.

The images from both previous methods provided spatial information on PpIX distribution across the tumor surface and adjacent tissue. Image analysis was performed using the Python programming language with the open-source library ImFun (Image Functions), which was developed by our group and is available at https://github.com/MarlonGarcia/imfun. The function `roi_stats` from this library was applied to select a region of interest within the images and compute statistical metrics from pixel intensities in the tumor region. The red channel of the widefield visible fluorescence images was used to quantify the PpIX fluorescence [24,62]. Since the widefield NIR fluorescence images had only one channel, the statistical analysis was performed on that channel, and PpIX fluorescence was quantified by the mean pixel intensity within the tumor region [62,67].

The third method, SSFS, employed a system consisting of a diode laser (408 nm), with an average power of 10 mW, coupled to a 600 μm Y-type optical fiber probe (BIF600-UV–VIS, Ocean Optics Inc., Dunedin, FL, USA) for simultaneous light delivery and fluorescence collection. For the excitation in 408 nm, long-pass filters at 420 nm (GG550, Schott North America Inc., Duryea, PA, USA) were used to eliminate backscattered excitation light. Fluorescence emission spectra were then acquired in the range of 400–800 nm using a spectrophotometer (USB 2000-FL, Ocean Optics Inc., USA) connected to a computer running OOIBase software (Ocean Optics, USA) for data acquisition [68,69]. For each animal, fluorescence spectra were collected from five distinct positions within the tumor region at each acquisition time point. The spectra were plotted and processed using Origin® software (OriginLab, USA). To minimize variations in fluorescence intensity caused by differences in fiber positioning or by skin heterogeneity among animals, the PpIX fluorescence peak at 630 nm was normalized against the endogenous skin fluorescence peak at 450 nm.

2.4.4. Ex vivo Confocal microscopy measurements

To assess the in-depth production and distribution of PpIX, confocal microscopy measurements were performed on tumor samples. Tumors were collected after 30, 60, and 120 min of DMNf or cream incubation, frozen, and stored at −80 °C before longitudinal sectioning into 30 μm-thick slices using a cryostat (Leica Biosystems, CM1850, UK).

Fluorescence images were acquired using a confocal microscope (Zeiss LSM780, Germany). A 405 nm diode laser was used for excitation, and fluorescence signals were collected in the 430–580 nm channel for endogenous skin fluorescence and in the 630–670 nm channel for PpIX fluorescence. Laser intensity, gain, and detection contrast parameters were standardized and maintained constant throughout acquisition. Data processing was performed in Python using the `roi_stats_in_depth` function from the ImFun library. Only the red channel (630–670 nm) corresponding to PpIX emission was analyzed. The algorithm enables manual delineation of the outermost skin surface and the deepest tumor boundary, then partitions the intervening region into equally spaced subregions (for our case, 30 regions were chosen). For each subregion, `roi_stats_in_depth` returns summary statistics, including mean fluorescence intensity, providing a depth-resolved measure of PpIX distribution and enabling correlation of surface and subsurface signals.

2.5. Statistical analysis

All values were expressed as mean±standard deviation, and statistical significance between groups was assessed using Tukey tests, with $\alpha \leq 0.05$ considered significant. Statistical calculations and visualizations were performed using the Paired Comparison Plot app from OriginLab (OriginLab Corporation, USA) software to compare paired datasets.

3. Results

3.1. Characterization of ALA-DMN

3.1.1. ALA-DMN structure and ALA concentration

Fig. 3a presents a SEM image of the tip array, which is the same for both DMN types, DMNe and DMNf, and highlights the tip uniformity and well-defined morphology, with dimensions consistent with those of the original molds (Fig. 3b). The final dried DMNe and DMNf patches, each containing a 1 cm tip array, are shown in Fig. 3c and 3–d, respectively.

An important consideration is that although the initial ALA concentration in the Gantrez-ALA formulation was 10% (w/w), the drying process of the DMN increased the concentration to 33%. This increase resulted from the reduction in DMN total mass from 140 mg to 42 mg, mainly due to the loss of water. For clinical protocols, the ALA concentration in cream formulations is typically 20% [10,13,14]. In previous work, Requena et al. (2022) reported an ALA concentration of 17% in dried DMN with a pyramidal design, fabricated from a formulation containing 5% ALA in an aqueous solution using the same polymer

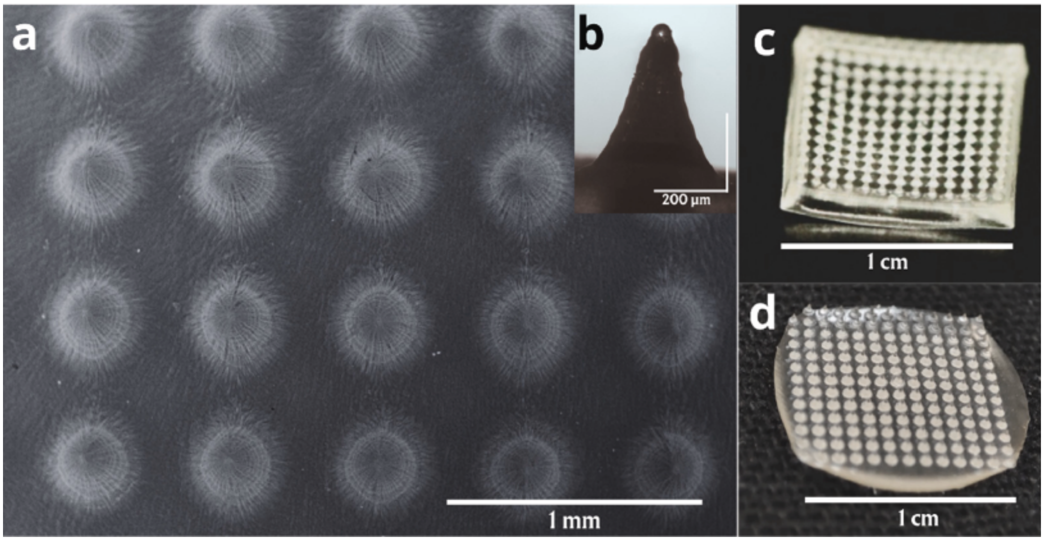

Fig. 3. (a) SEM image showing the top view of the tip array of both DMN types. (b) Microscopic image of a single tip with a well-defined conical profile. Complete array of (c) DMNe, and (d) DMNf.

employed in this study. The higher ALA concentration achieved in the present DMN (33%) could enhance the transdermal delivery of ALA to target cells (i.e., increased drug bioavailability), potentially reducing the required incubation times and thereby improving the overall efficiency of PDT treatment.

3.1.2. In vitro insertion test of DMN

By evaluating both the number of parafilm layers penetrated and the number of holes generated in each layer by the DMN, we observed that the results were independent of the formulation used in DMN preparation, namely Gantrez-DMN or ALA-DMN. This finding indicates that the addition of ALA to the formulation did not affect either the drying process or the mechanical resistance of the DMN. However, the results did differ when the DMNs were compared according to their structural design, i.e., DMNf versus DMNe. As shown in Fig. 4a and 4b, the number of holes at different depths created by DMNf and DMNe differed. DMNf produced a higher percentage of holes in the first two layers, with tip insertion occurring mainly in the center. In contrast, DMNe achieved deeper penetration (up to ~625 μm), with tip insertion occurring primarily at the edges.

Although DMNe penetrated more layers, the percentage of holes decreased from 95% in the first layer (125 μm) to 65% in the second layer (250 μm), whereas DMNf achieved 100% penetration in the first layer and 96% in the second layer (Fig. 4c). In a previous study, DMNs prepared with a similar Gantrez-ALA formulation containing 5% ALA but featuring pyramidal tips showed only 80% tip penetration at a depth of 250 μm [24]. The DMNf patches fabricated in the present study demonstrated superior penetration performance compared to that previously reported. These results highlight tip geometry as a critical structural factor for effective DMN insertion. This finding is consistent with Li et al. (2020), who reported that conical tip geometries possess superior mechanical properties compared to pyramidal designs [48].

Notably, our study revealed a critical insight that despite both DMN designs sharing identical tip formats and achieving sufficient penetration depth (250 μm) to reach the dermis (human epidermis: 180–200 μm) [70], the presence or absence of an outer wall structure significantly altered the penetration pattern. This suggests that MN array design, beyond tip geometry alone, can influence drug distribution mechanics, even when targeting the same tissue layer.

3.1.3. Assessment of Gantrez–ALA interaction by MALDI-TOF

ALA is a molecule that can be combined with other polymers; however, ALA-polymer interaction could result in differences in drug stability, biocompatibility, and controlled release kinetics [20,71]. The mass spectra of films containing Gantrez and ALA (Fig. 4d) were evaluated, revealing the characteristic ALA (m/z = 132.028), acetaminophen (m/z=152.118), and Gantrez (m/z=172.137) peaks. This indicates that ALA did not aggregate with Gantrez and remained detectable using this technique. Maintaining a drug in a non-aggregated state within a polymeric matrix ensures uniform distribution, as illustrated in the inset of Fig. 4d, enables more precise control over drug release, and preserves its chemical integrity. The ALA calibration curve used to quantify ALA concentration was linear across the tested range, with a mean correlation coefficient of R^2 = 0.99697. Based on this curve, the ALA mass calculated in the thin film was 8.8±1.4 mg, which corresponds closely to the initial amount of ALA used in the formulation for thin-film preparation (10 mg). These results indicate that the ALA content was largely preserved, with minimal mass loss, and that the molecules remained stable, showing no signs of aggregation and a homogeneous distribution within the films.

3.2. ALA-DMN biocompatibility in A431 cells

The cell viability assays confirmed that the solution obtained by diluting the Gantrez-DMN did not reduce cell viability at any concentration (10, 5, 2.5, 1, and 0.1 mg/mL) (Fig. 4e). The enhanced cell viability at the lower concentrations of 1 and 0.1 mg/mL can be explained by the biomimetic properties of some polymers. These properties emulate the native extracellular matrix by offering mechanical support and essential biochemical cues, which collectively create a conducive microenvironment for cell adhesion and proliferation [72]. In contrast, the solution obtained by diluting the ALA-DMN did not produce statistically significant differences among the groups (Fig. 4f). These findings suggest that while lower concentrations of the Gantrez films may support cell proliferation, the incorporation of 10% ALA does not exert a statistically significant effect on cell viability.

Previous studies have also evaluated the biocompatibility of Gantrez AN-139 as a polymeric material for drug delivery. Donnelly et al. (2012) investigated its cytotoxicity using 3-(4,5-dimethylthiazol-2-yl)-2,5-diphenyl tetrazolium bromide (MTT) viability assays in fibroblasts (Balb/3T3), keratinocytes (NTERT-1), and a 3D keratinocyte skin model. These studies were complemented by skin irritancy tests, which

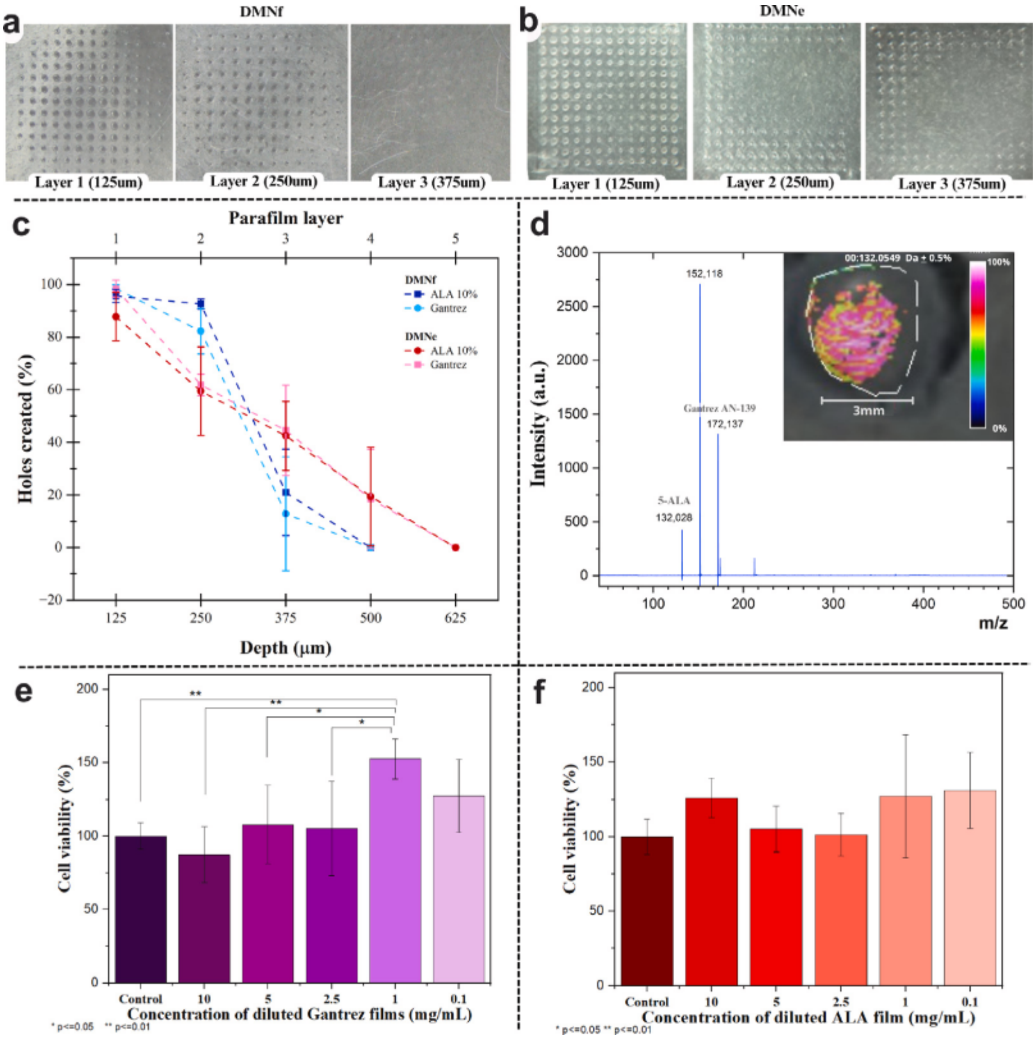

Fig. 4. Images of parafilm layers showing holes created by (a) DMNf and (b) DMNe. (c) Percentage of holes created after insertion tests performed by the DMNs. Each parafilm layer corresponds to a depth of 125 µm. (d) MALDI-TOF mass spectra from the films containing ALA (*m/z*=132) and Gantrez AN-139 (*m/z*=172). The inset in this figure shows the MALDI imaging of ALA distribution within a thin circular film (3 mm in diameter, 1 mm in thickness). The color bar represents the intensity of ALA distributed in the delimitated area, with 0% shown in black and 100% in white. (e–f) Cell viability percentage of A431 cell line after incubation for 24 h with solutions obtained by diluting the (e) Gantrez-DMN and (f) ALA-DMN patches in culture medium at a dose of 10, 5, 2.5, 1, 0.1 mg/mL. Group comparisons were performed using the Tukey test ($\alpha \leq 0.05$ was considered statistically significant).

demonstrated no cytotoxic effects and no irritant response, thereby confirming the safety and biocompatibility of Gantrez with skin tissue [73]. De Lima et al. (2024) further assessed the cytotoxicity of the polymer using MTT assays in human lung epithelial cells (A549) and lung fibroblasts (MRC-9) cultured in DMEM, with Gantrez tested at 0.2% (w/v) or 2 mg/mL. Their results demonstrated that this concentration did not induce cytotoxicity in the studied cell lines [74]. Collectively, these findings reinforce the potential of DMN formulations for biomedical applications, highlighting their safety and favorable interactions with cells even when loaded with ALA.

3.3. *In vivo PDT effects*

3.3.1. *DMN insertion and dissolution*

When the tumors reached the desired volume (Fig. 5a), PDT was applied. Prior to illumination, qualitative observations were performed to verify MN tip perforation and to compare the insertion performance of both DMNe and DMNf patches with that of the cream treatment (Fig. 5b–d). Visible microholes on the tumor surface confirmed successful microneedle penetration into the tissue for both DMN types. The tip dissolution after 60 min demonstrated ALA release directly into the tumor. The combination of sufficient penetration depth and progressive dissolution ensures ALA delivery to deeper tumor layers, which is essential for enhancing PpIX production. However, the DMN array did not achieve complete tip dissolution within the incubation period, a factor that may limit drug delivery efficiency. This finding highlights the need for further formulation optimization to improve dissolution kinetics and maximize therapeutic outcomes. Importantly, no external agents were employed to accelerate dissolution, ensuring that the assessment reflects the intrinsic performance of the MN formulation under standard conditions.

Previous studies have reported variable dissolution times for DMN, ranging from minutes to hours, depending on polymer composition and DMNs solubility in water. For instance, McCrudden et al. (2014) developed DMN with 30% Gantrez for controlled ibuprofen release, achieving a dissolution time of 5 min in a rat skin model, with effective release extending from 4 to 24 h [75]. Similarly, Iyer et al. (2021) emphasized the importance of skin hydration in DMN insertion tests using hyaluronic acid (HA) as a hydrophilic polymer base [76]. Their findings demonstrated significant differences in DMN dissolution across untreated, dehydrated, and tape-stripped skin models, with enhanced hydration improving dissolution and tip performance.

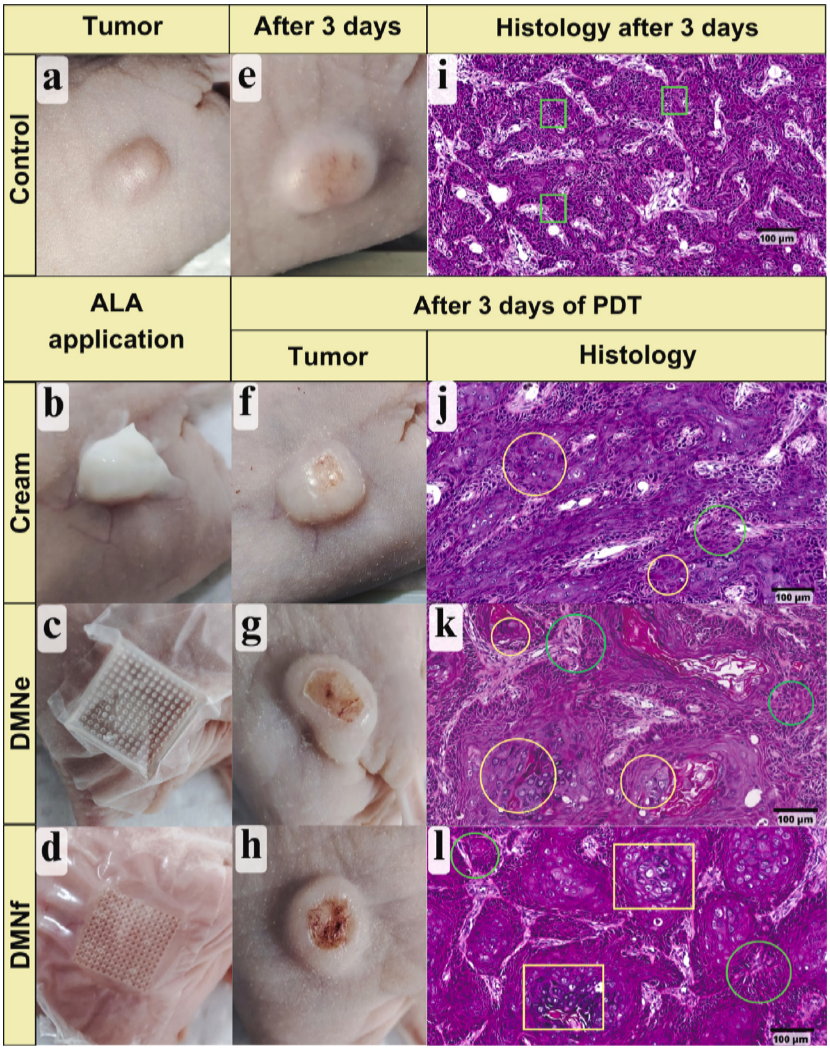

Fig. 5. Representative images of murine nodular tumors with an initial volume of 15–25 mm^3 in (a) the control group, and after ALA application in (b) the cream, (c) DMNe, and (d) DMNf groups. Representative images of (e) control tumor 3 days after the starting point, and treated tumors 3 days post-PDT in (f) the cream, (g) DMNe, and (h) DMNf groups. H&E-stained histological sections of (i) control tumor 3 days after the starting point, showing mitotic foci (green squares); and treated tumors 3 days post-PDT in (j) the cream group (showing intratumoral infiltration in green and metaplasia foci in yellow), (k) the DMNe group (showing diffuse intratumoral infiltrations in green circles, necrosis and hemorrhage in yellow squares, and additional metaplasia foci in yellow circles), and (l) the DMNf group (showing intratumoral infiltration in green and metaplasia foci in yellow).

3.3.2. Tumor damage generated by PDT sub-dose

Tumor damage was assessed 72 h after sub-dose PDT through both macroscopic and histological analyses and compared with the control group (Fig. 5e).

Macroscopically, the cream-treated group exhibited smaller lesion areas and shallower damage (Fig. 5f), whereas the DMN groups showed larger affected regions, indicating greater damage. Among them, DMNf (Fig. 5h) induced more extensive and deeper tumor damage than both the cream and DMNe groups (Fig. 5g), suggesting enhanced PpIX production, thereby resulting in a stronger PDT effect.

Histological analysis revealed no signs of damage in the control group (Fig. 5i), which displayed only mitotic activity consistent with tumor progression. In contrast, treatment groups presented inflammatory infiltrates (green circles), necrosis and hemorrhage (yellow squares), and foci of squamous metaplasia (yellow circles) as markers of tumor damage. Inflammatory infiltrates were observed in all PDT-treated groups, with the DMNf group showing the most pronounced response (Fig. 5l). Squamous metaplasia was detected across all treated tumors, with DMNf displaying more foci together with hemorrhage and extensive tissue damage, further supporting its superior PDT efficacy.

3.3.3. Superficial PpIX production and photobleaching post-PDT

Visible fluorescence imaging. As shown in Fig. 6a, before ALA application (0 min), this method revealed endogenous fluorescence in green tones originating from both the tumor-overlying skin and the surrounding tissue in all three experimental groups (cream, DMNe, and DMNf). After 60 min of ALA application via cream, DMNe, or DMNf, PpIX accumulation in the tumor region became evident in red tones, corresponding to PpIX fluorescence at 635 nm upon excitation with 400 ± 10 nm light. Since the cream application was carefully positioned directly on the tumor, minimizing contact with the surrounding skin, the fluorescence detected around the tumor was likely due to cream diffusion into the skin, which is facilitated by the thinner tissue layers of murine skin. The DMNe group exhibited more selective PpIX deposition, whereas a broader fluorescence distribution was particularly noticeable in the DMNf group, potentially due to better indentation. The intensity in the red channel of the fluorescence images was normalized and correlated with the PpIX fluorescence intensity. These normalized data were grouped and presented as a box plot in Fig. 6b, showing considerable fluctuations, likely due to variations in superficial PpIX synthesis and differences in individual animal metabolism. After 60 min of ALA incubation, the DMNf group displayed the highest mean

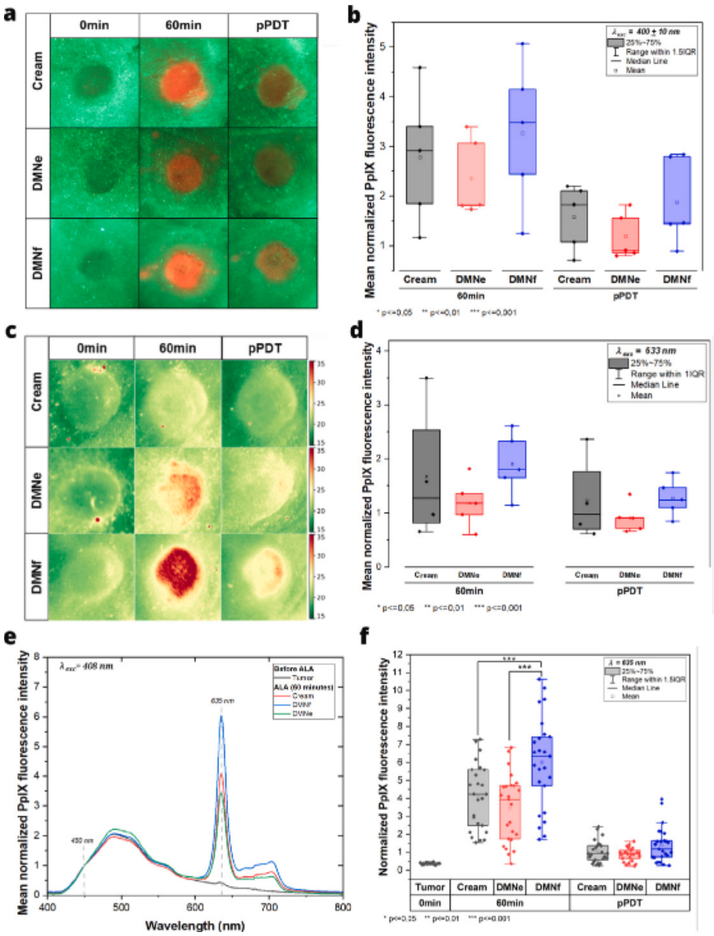

Fig. 6. Visible PpIX fluorescence method: (a) Representative widefield fluorescence images (shown in true colors) of tumors for each experimental group, collected in the visible range before ALA administration (0 min), after 60 min of incubation (60 min), and following PDT (pPDT). (b) Box plot graph of normalized PpIX fluorescence intensity for the DMN and cream groups at the same time points. **NIR PpIX fluorescence method**: (c) Representative widefield fluorescence images (false-color image) of tumors for each experimental group, acquired in the NIR range at three time points (0 min, 60 min, and pPDT). Green indicates low fluorescence intensity and red indicates high intensity, as shown in the color bar. (d) Box plot of mean normalized PpIX fluorescence intensity for the DMN and cream groups at the same time points. **SSFS method:** (e) Mean PpIX fluorescence spectra for each experimental group at two time points (0 min and 60 min). (f) Box plot of mean normalized PpIX fluorescence intensity for the DMN and cream groups at three time points (0 min, 60 min, and pPDT). Group comparisons were performed using the Tukey test ($\alpha \leq 0.05$ was considered statistically significant).

fluorescence signal, followed by the cream group and, lastly, the DMNe group. This indicates that the DMNe array indentation was not optimal during insertion, directly affecting tumor contact and ALA release. After PDT, the normalized PpIX fluorescence intensity decreased in all groups, confirming PpIX consumption following light application.

NIR fluorescence imaging. The images are shown in Fig. 6c, with a color map applied for improved visualization. Before ALA application, endogenous fluorescence was shown in both the skin and tumor in green tones. After 60 min of ALA incubation, PpIX accumulation was evident represented in red tones, with the high NIR fluorescence intensities in the tumor region, excited with 635 nm light. The DMNf group exhibited greater PpIX deposition in the tumor region compared to the cream and DMNe groups. The pixel intensity in the NIR fluorescence images was normalized and correlated with the PpIX fluorescence intensity (Fig. 6d). Unlike the DMN groups, the data showed considerable fluctuations in the cream group. After 60 min of ALA incubation, the DMNf group exhibited significantly higher mean fluorescence signal than the DMNe and cream groups, suggesting that the DMNf patch achieved better tip insertion and, consequently, enhanced ALA delivery and PpIX synthesis. Compared to the previous method, the NIR spectral region exhibited a substantial reduction in skin absorption and scattering coefficients, allowing for deeper light penetration into the tissue and enhancing the visualization and assessment of fluorescence signals within the tumor. Similar to the previous method, PDT led to a decrease in normalized PpIX fluorescence intensity across all groups.

Steady-state fluorescence spectroscopy. As shown in Fig. 6e, before ALA administration, the tumor exhibited higher fluorescence intensity within the 400–600 nm range, attributable to the endogenous fluorescence of the animal skin, while the signal at 635 nm was minimal. After 60 min of ALA administration, via cream (red line), DMNf (blue line), or DMNe (green line), mean fluorescence intensity within the 400–600 nm range showed minimal variation, with a marked increase around 635 nm, corresponding to the characteristic PpIX fluorescence band. When comparing the PpIX fluorescence intensity (points in Fig. 6f) collected after ALA incubation for each application method, considerable fluctuations were observed, likely due to the specific region of fluorescence collection and individual animal metabolism. Comparing the normalized PpIX fluorescence intensity at 635 nm, the DMNf group produced a higher signal than the cream and DMNe groups. After PDT, no significant differences in fluorescence signals were observed between the protocols, all of which showed low-intensity values comparable to the tumor's endogenous fluorescence. These findings suggest that the selected light parameters were effective in reducing the detectable PpIX fluorescence under violet-light excitation, which has limited tissue penetration.

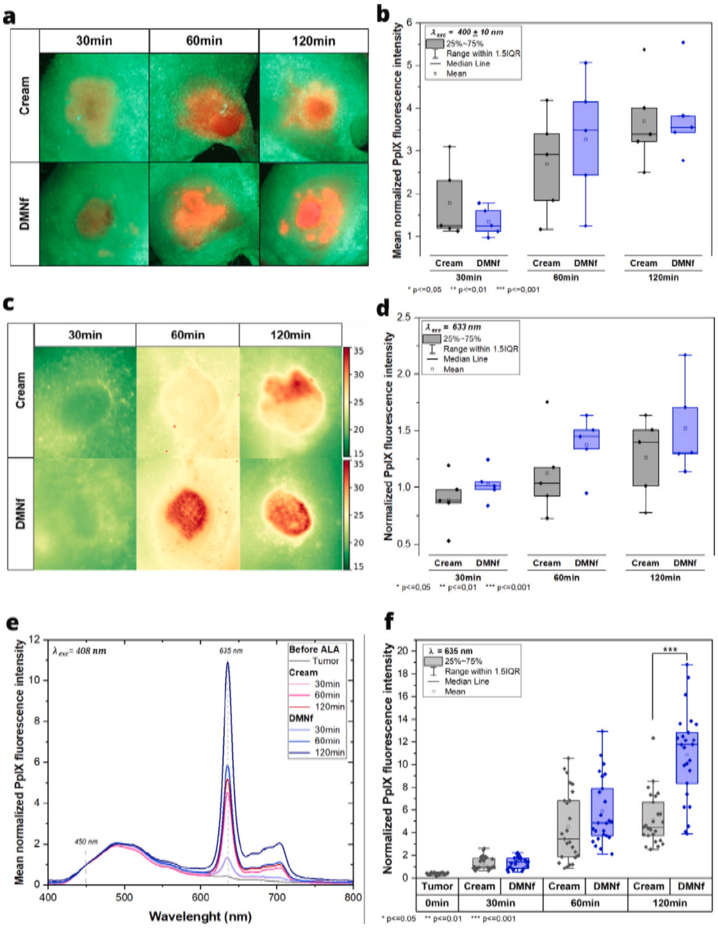

Fig. 7. **Visible PpIX fluorescence method:** (a) Representative widefield fluorescence images (true colors) of tumors from each experimental group, collected in the visible range at three time points (30, 60, and 120 min). (b) Box plot showing PpIX fluorescence intensity differences between DMNf and cream groups at the same time points. **NIR PpIX fluorescence method:** (c) Representative widefield fluorescence images (false-color) of tumors from each experimental group, acquired in the NIR range at three time points (30, 60, and 120 min). Green indicates low fluorescence intensity and red indicates high intensity, as shown in the color bar. (d) Box plot showing PpIX fluorescence intensity differences between DMNf and cream groups at the same time points. **SSFS method:** (e) Mean PpIX fluorescence spectra comparing ALA application by cream (red lines) and DMNf (blue lines) at three time points (30, 60, and 120 min). (f) Box plot comparing normalized PpIX fluorescence intensity at the 635 nm peak for cream and DMNf groups at the same time points. Group comparisons were performed using the Tukey test ($\alpha \leq 0.05$ was considered statistically significant).

The ALA delivery protocols (i.e., Cream, DMNf, DMNe) used in this PDT study employed a 60-minute incubation period, consistent with previous work where cream [24,77] and DMNs [24,78] were applied for ALA administration. In the present investigation, however, additional incubation times (30, 60, and 120 min) were evaluated to determine the optimal PpIX production using cream or DMNf, which demonstrated superior performance.

3.3.4. Superficial PpIX production at different ALA incubation periods

Visible fluorescence imaging. Fig. 7a presents the data obtained from visible PpIX fluorescence measurements, where images were collected over time using the LINCE system. The fluorescence values were normalized and grouped for presentation as a box plot in Fig. 7b. After 30 min of incubation, no significant difference was observed between the cream and DMNf groups, likely due to the limited dissolution time of the microneedles. At 60 min, the DMNf group exhibited a more localized PpIX accumulation around the tumor area, although the difference was not statistically significant. By 120 min, no variation in superficial fluorescence intensity was detected between the groups. Overall, these results represent the superficial PpIX fluorescence signal.

NIR fluorescence imaging. Fig. 7c shows wide-field images with excitation at 630 nm and collection in the near-infrared. At 60 and 120 min, the images obtained using DMNf displayed higher fluorescence intensity than those obtained with the cream, as well as a more homogeneous distribution within the tumor region. The data obtained with the near-infrared system (Fig. 7d) show an increase in PpIX production as the incubation time increases for both applications. A higher fluorescence signal was observed for the DMNf group at 60 and 120 min compared to the cream under the same incubation conditions. As this technique detects fluorescence signals originating from deeper tissue layers, these results indicate that the precursor was delivered to greater depths with the DMNf, enabling enhanced PpIX production and distribution compared to the topical cream application. These spatial findings on PpIX fluorescence distribution and intensity further support and complement the results obtained from the visible widefield fluorescence imaging.

Steady-state fluorescence spectroscopy. Fig. 7e shows an increase in mean PpIX fluorescence intensity with longer incubation times; however, the signal increase from 60 to 120 min was greater for the DMNf group than for the cream group. This may be related to the minimum time required for ALA release, subsequent PpIX formation, and accumulation. Moreover, the diffusion of molecules through DMNs differs from that of cream, owing to the dissolution process and the degree of molecular bonding within the polymer matrix. Fig. 7f presents the normalized PpIX fluorescence intensity at the 635 nm emission

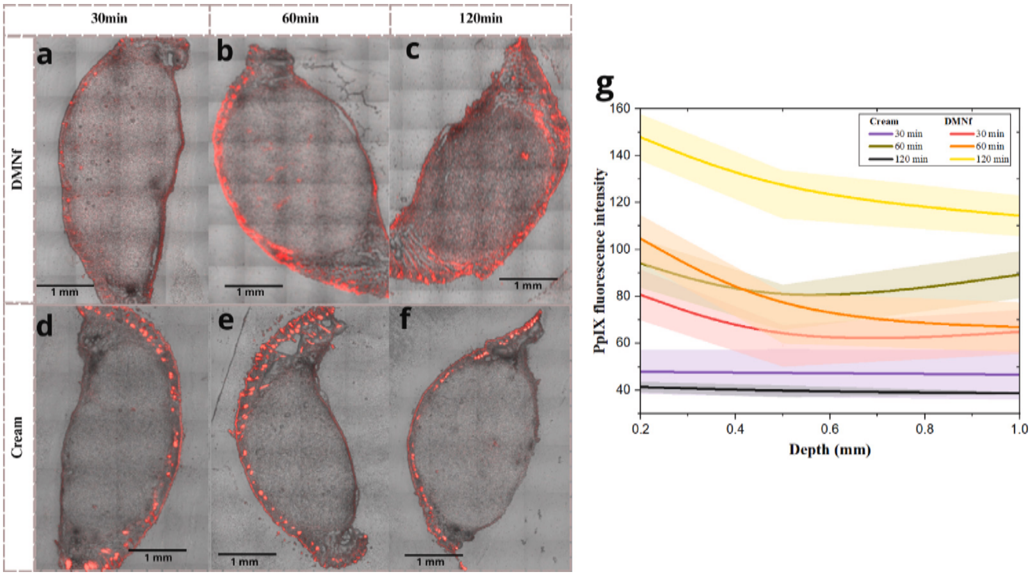

Fig. 8. Red PpIX fluorescence images overlaid on brightfield images obtained from the (a–c) DMNf and (d–f) cream groups, after 30 min, 60, and 120 min, respectively. (g) Mean red-channel fluorescence intensity as a function of tumor depth, comparing ALA delivery via cream and DMNf at different time points (30, 60, and 120 min). Each curve was constructed from multiple points representing the mean value for n = 5 per group, with the shaded area indicating data dispersion.

peak across the different time points. At 30 min, the fluorescence signal remained weak, suggesting limited PpIX formation on the tumor surface. After 60 min, an increase in fluorescence intensity was observed relative to the earlier time point. By 120 min, this trend was further accentuated, particularly in the DMNf group, where the fluorescence increase was statistically significant compared to the cream, despite exhibiting more variability as reflected by a larger standard deviation.

3.3.5. In-depth PpIX production and distribution

Confocal fluorescence microscopy images were analyzed to assess the in-depth production and distribution of PpIX. Fluorescence images overlaid on transmission light microscopy of representative tumors are shown in Fig. 8a–c for the DMNf group and Fig. 8d–f for the cream group at three different incubation times (30, 60, and 120 min). These images reveal a more intense signal in the deeper tumor layers for the DMNf group compared with cream by the time, indicating that intradermal delivery improved PS penetration and distribution compared with topical application. After 120 min of ALA incubation, the PpIX fluorescence intensity throughout the tumor became more pronounced, indicating that DMNf achieved superior in-depth delivery compared to the cream (Fig. 8c).

The mean fluorescence intensity shown in Fig. 8g was measured at depths ranging from 0.2 mm to 1 mm. At all depths evaluated, PpIX fluorescence intensity was higher when ALA was delivered via DMNf, indicating superior effectiveness at greater depths and consistent release over time. For both cream and DMNf, the increase in PpIX fluorescence between 30 and 60 min was modest; however, a significant rise was observed at 120 min. At this time point, the DMNf group exhibited significantly higher PpIX fluorescence compared with the cream application.

In summary, the data demonstrate that cream-based ALA delivery results in optimal PpIX formation after 60 min of incubation; however, its diffusion into deeper tumor layers becomes less effective over longer periods. In contrast, the DMNf group exhibited superior efficacy at greater depths (up to 1 mm), with significantly higher PpIX fluorescence intensity after 120 min. This enhanced intratumoral distribution, compared with topical cream application, suggests that DMNf not only overcomes the limitations of conventional PDT approaches but also holds strong potential to improve therapeutic outcomes in thicker and more treatment-resistant skin lesions.

4. Discussion

The approved clinical PDT protocols for the treatment of superficial non-melanoma skin cancer involve the topical application of ALA or MAL. Some clinical protocols include applying ALA or MAL cream after a debulking procedure, in which crusts and superficial material are removed to enhance cream permeation and improve treatment effectiveness [79,80]. This debulking step may also positively influence microneedle application, as the presence of residual fluid within the lesion—even after excess blood is removed—could facilitate DMN dissolution and potentially reduce the incubation time required in clinical protocols. Consequently, ALA delivery via cream or DMNs in an intact tumor may differ from that in a debulked lesion. In our experiments, the amount of cream applied was standardized to form a thick layer over the tumor surface, ensuring consistent and uniform availability; however, no debulking procedure was performed in the animals to avoid introducing additional variables that could interfere with the permeation analysis.

Topical creams encounter significant challenges in permeating the skin, primarily due to the stratum corneum. Furthermore, their application requires a defined period for diffusion through tumor layers and subsequent intracellular PpIX synthesis. In comparison, DMN introduces an additional phase before drug release, which is the DMN dissolution, after which ALA is liberated and initiates PpIX production upon cellular uptake. As a result, the overall time required for PpIX formation and accumulation is longer for DMNs than for creams, owing to dissolution kinetics influenced by intrinsic factors such as skin physiology and hydration, and extrinsic factors such as relative humidity. Optimizing these parameters is essential to enhancing DMN efficacy. The cream and DMN formulations tested in this study exhibited important differences. Both contained 10% ALA; however, the clinically used cream also included EDTA (0.15%), which prevents iron binding to PpIX during heme synthesis, thereby enhancing PpIX accumulation [55]. This property likely provides an advantage over DMNs [81,82]. Incorporating EDTA directly into the DMN formulation was not feasible due to molecular interactions between the polymer and other additives, which interfered with the drying process and compromised DMN stability [83]. Despite this limitation, the comparable and, in some cases, superior outcomes observed with DMNs highlight their robust performance and considerable potential for further optimization.

Gantrez AN-139 is a highly water-soluble polymer, but our formulation presented a slow dissolution rate. Previous ex vivo data from our group demonstrated that formulations comprising 20% Gantrez and 5% ALA dissolved completely within approximately 15 min; this rapid dissolution profile was not directly translatable to the in vivo environment [24]. In this study, complete dissolution *in vivo* was not achieved within the first hour, with the most substantial dissolution observed at the 120 min time point. This may be explained by the interactions between the zwitterionic properties of ALA and the Gantrez AN-139 polymer, which are likely to enhance the solubility of ALA through electrostatic bonding between its amino group and the carboxylate groups in the polymer, resulting in a homogeneous distribution within the formulation [84,85]. While this interaction improves solubility, it also amplifies the hygroscopic nature of the polymer, potentially compromising its mechanical stability after drying. Consequently, proper storage in a low-humidity environment is essential to preserve the microneedle arrays' structural integrity. Interestingly, this increased hygroscopicity could present an advantage during application. The enhanced dissolution properties may improve drug release in humid environments, such as in hydrated tumors or after curettage. This characteristic suggests a potential dual benefit: optimizing drug distribution while adapting to the specific conditions of the treatment site. Further studies are needed to balance these properties to ensure stability during storage and efficient delivery during application.

Conventional topical PDT is often limited to superficial lesions due to the significant barrier imposed by the stratum corneum and the hydrophilic physicochemical properties of ALA, which collectively lead to inefficient drug delivery [40]. To improve topical PDT outcomes in thicker lesions, non-invasive strategies are under investigation, including the combination of light with deeper-penetrating excitation sources such as low-intensity ultrasound [86], the use of thermogenic and vasodilators agents [87] to increase PpIX production, and the use of intradermal delivery approaches to enhance drug penetration [65]. In this sense, this work prepared two types of DMNs with a formulation containing initially 10% ALA and 20% Gantrez® AN-139 polymer in water as alternative intradermal delivery platforms. The superior PpIX accumulation observed with the DMNf formulation, compared to both the cream and DMNe applications, strongly correlates with enhanced therapeutic efficacy in deeper tumor regions and within a shorter time frame. These *in vivo* findings are in strong agreement with the prior *in vitro* insertion studies. Another goal in topical PDT is to shorten treatment duration by reducing the drug–light interval. So, the improvement of drug release efficiency may be implemented by additional protocols such as skin hydration or formulation adjustments. Requena et al. (2021) applied localized heating at 40 °C during the first 15 min of DMN insertion in a tumor model, which promoted greater dissolution compared with non-heated protocols; however, complete dissolution was not achieved [24]. Kathuria et al. (2020) investigated DMNs formulated with polyvinylpyrrolidone (PVP) and dissolution modifiers, reporting dissolution times ranging from 45 min to 48 h. They observed an inverse relationship between dissolution rate and penetration depth, with optimal penetration achieved using a PVP–methacrylic acid (MAA) formulation that dissolved in 8 h in a skin model [88]. These findings underscore the potential of DMNs as a promising alternative to creams, offering advantages in controlled release and targeted delivery, particularly for deeper tissues. Further optimization of DMN formulations for scalability and application protocols could significantly improve their therapeutic efficacy.

Whereas the broader DMN field faces significant challenges in scalability, reproducibility, and sterilization, the approach detailed herein provides tangible solutions to these very issues [89,90]. Scalability and low cost were central to the design, achieved through the use of inexpensive polymers and locally fabricated molds with 3D-printed master templates, which are substantially more cost-effective than expensive imported commercial options. This work also directly addresses reproducibility which represents an industry challenge, by validating an optimized drying protocol (25 °C for 72 h) that ensures homogeneous evaporation and critical DMNs rigidity. Furthermore, in response to the complex problem of sterility, this study can be complemented with a previous study with ozone decontamination, a crucial step that ensured the microbial safety of ALA-loaded DMNs without compromising polymer properties or drug stability [59]. These advances in low-cost, reproducible manufacturing, coupled with validated decontamination and the minimally invasive, painless application of DMNs, position this technology as a highly promising and cost-effective alternative to conventional treatments.

Given that patient variability in skin characteristics remains an inherent challenge affecting both DMNs and conventional topical formulations, future research must focus on optimizing treatment for individual physiology while extending the scope of the current work. Consequently, essential next steps should integrate detailed investigations of microneedle dissolution kinetics, long-term immune and toxicity profiles, and patient acceptability with the establishment of industrial-scale manufacturing protocols, all of which are necessary prerequisites for proceeding to formal clinical trials.

5. Conclusion

This study introduces a novel DMN formulation designed for enhanced intradermal drug delivery. Each array contained a 10% ALA, demonstrating sufficient mechanical strength to achieve 90% insertion efficiency to a depth of approximately 250 μm with no significant deformation. Biocompatibility was validated through *in vitro* assays using a tumor cell line. Compared to topical cream, the DMN enables more effective ALA delivery, resulting in greater PpIX accumulation in deeper tumor regions. These results underscore DMN as a promising platform for intradermal delivery due to its scalable fabrication, low production cost, and potential for clinical translation. This approach may be particularly advantageous for PDT of nodular skin lesions. Nonetheless, further studies on MN dissolution dynamics are needed to ensure complete drug release and to enable the standardization of application protocols.

CRediT authorship contribution statement

Dianeth Sara Lima Bejar: Writing – original draft, Writing – review & editing, Visualization, Validation, Methodology, Investigation, Formal analysis, Data curation. **Michelle Barreto Requena:** Writing – review & editing, Visualization, Validation, Formal analysis, Conceptualization. **Mirian Denise Stringasci:** Review & editing, Methodology, Investigation. **Marlon Rodrigues Garcia:** Review & editing, Validation, Software, Formal analysis, Data curation. **Erika Toneth Ponce Ayala:** Writing – review & editing, Validation, Formal analysis, Data curation. **Juliana Cristina Barreiro:** Review & editing, Methodology, Formal analysis. **Sebastião Pratavieira:** Review & editing, Visualization, Validation, Investigation, Formal analysis. **Vanderlei Salvador Bagnato:** Review & editing, Supervision, Resources, Project administration, Funding acquisition, Conceptualization.

Funding

This research was funded part by the Coordination for the Improvement of Higher Education Personnel (CAPES, fellowship no. 88887.703138/2022-00), São Paulo Research Foundation (FAPESP: 2013/07276-1 (CEPOF), 2014/50857-8 (INCT), fellowships no. 2022/10860-6, 2023/04209-3, and, 2025/11565-6), National Council for Scientific and Technological Development (CNPq, 465360/2014-9, 408468/2024-6); and by grants from the Cancer Prevention and Research Institute of Texas, United States (CPRIT, RR220054), the Governor's University Research Initiative (GURI, 01-2023), and the Chancellor's Research Initiative (CRI).

Declaration of competing interest

The authors declare that they have no known competing financial interests or personal relationships that could have appeared to influence the work reported in this paper.

Acknowledgments

We thank the Brazilian Nanotechnology National Laboratory (LNNano) at the Brazilian Center for Research in Energy and Materials (CNPEM) for manufacturing the molds (Project n° 20220606); Dr. Kelly Tasso de Paula from São Carlos Institute of Physics, University of São Paulo (IFSC-USP) for the SEM imaging, Dr. Aline M. dos Santos and Prof. Marlus Chorilli from the School of Pharmaceutical Sciences, Sao Paulo State University (Unesp) for their collaboration with Texture Analyzer, and São Carlos Institute of Chemistry, University of São Paulo (IQSC-USP) for the MALDI-TOF analyses.

Data availability

Data will be made available on request.

References

[1] National Comprehensive Cancer Network, NCCN guidelines: Basal cell skin cancer, 2025, https://www.nccn.org/guidelines/guidelines-detail?category=1&id=1416. (Accessed 03 September 2025).

[2] M.C. Cameron, E. Lee, B.P. Hibler, C.A. Barker, S. Mori, M. Cordova, K.S. Nehal, A.M. Rossi, Basal cell carcinoma: Epidemiology; pathophysiology; clinical and histological subtypes; and disease associations, J. Am. Acad. Dermatol. 80 (2) (2019) 303–317, http://dx.doi.org/10.1016/J.JAAD.2018.03.060.

[3] World Cancer Research Fund, Skin cancer, 2025, https://www.wcrf.org/preventing-cancer/cancer-types/skin-cancer/. (Accessed 01 September 2025).

[4] American Cancer Society, Key statistics for basal and squamous cell skin cancer, 2025, https://www.cancer.org/cancer/types/basal-and-squamous-cell-skin-cancer/about/key-statistics.html. (Accessed 01 September 2025).

[5] H.H. Buzzá, L.T. Moriyama, J.D. Vollet-Filho, N.M. Inada, A.P. da Silva, M.D. Stringasci, M.B. Requena, C.T. de Andrade, K.C. Blanco, D.P. Ramirez, C. Kurachi, A.G. Salvio, V.S. Bagnato, Overall results for a national program of photodynamic therapy for basal cell carcinoma: A multicenter clinical study to bring new techniques to social health care, Cancer Control 26 (1) (2019) http://dx.doi.org/10.1177/1073274819856885.

[6] L. Themstrup, G. Jemec, Chapter 6 - optical coherence tomography for skin cancer and actinic keratosis, in: M.R. Hamblin, P. Avci, G.K. Gupta (Eds.), Imaging in Dermatology, Academic Press, Boston, 2016, pp. 59–67, http://dx.doi.org/10.1016/B978-0-12-802838-4.00006-6.

[7] E. Natelauri, A. Jghamadze, Radiation therapy for basal cell skin cancer, in: Skin Cancer, IntechOpen, Rijeka, 2025, http://dx.doi.org/10.5772/intechopen.1004362.

[8] E. Yosefof, N. Kurman, D. Yaniv, The role of radiation therapy in the treatment of non-melanoma skin cancer, Cancers 15 (9) (2023) http://dx.doi.org/10.3390/cancers15092408, URL https://www.mdpi.com/2072-6694/15/9/2408.

[9] S.S. Akella, J. Lee, J.R. May, C. Puyana, S. Kravets, V. Dimitropolous, M. Tsoukas, R. Manwar, K. Avanaki, Using optical coherence tomography to optimize Mohs micrographic surgery, Sci. Rep. 14 (1) (2024) 8900.

[10] H.H. Buzzá, A.P.d. Silva, J.D. Vollet Filho, D.P. Ramirez, J.R. Trujillo, N.M. Inada, L.T. Moriyama, C. Kurachi, V.S. Bagnato, Photodynamic therapy: Progress toward a scientific and clinical network in Latin America, Photodiagnosis Photodyn. Ther. 13 (2016) 261–266, http://dx.doi.org/10.1016/J.PDPDT.2015.08.004.

[11] P. Calzavara-Pinton, C. Zane, M. Arisi, P.-A. Hamon, N.T. Tanova, Evaluation of the costs of topical treatments for actinic keratosis based on lesion response and the affected area, G. Ital. Dermatol. Venereol. 153 (6) (2018) 764–775.

[12] B.C. Wilson, M.S. Patterson, The physics, biophysics and technology of photodynamic therapy, Phys. Med. Biol. 53 (9) (2008) R61, http://dx.doi.org/10.1088/0031-9155/53/9/R01.

[13] N.J. Collier, L.E. Rhodes, Photodynamic therapy for basal cell carcinoma: The clinical context for future research priorities, Molecules 25 (22) (2020) 5398, http://dx.doi.org/10.3390/MOLECULES25225398.

[14] M. Chen, A. Zhou, A. Khachemoune, Photodynamic therapy in treating a subset of basal cell carcinoma: Strengths, shortcomings, comparisons with surgical modalities, and potential role as adjunctive therapy, Am. J. Clin. Dermatol. 25 (1) (2024) 99–118, http://dx.doi.org/10.1007/S40257-023-00829-W/METRICS.

[15] G. Balakirski, P. Lehmann, R.M. Szeimies, S.C. Hofmann, Photodynamic therapy in dermatology: established and new indications, JDDG: J. Dtsch. Dermatol. Ges. 22 (12) (2024) 1651–1662, http://dx.doi.org/10.1111/DDG.15464.

[16] British Association of Dermatologists, Service guidance and standards for photodynamic therapy (PDT): 2023 update, 2023, https://cdn.bad.org.uk/uploads/2024/07/17112016/PDT-Service-Guidance-and-Standards-2023-Update.pdf. Updated October 2023; (Accessed 03 September 2025).

[17] L.C. Gomes-da Silva, L.G. Arnaut, et al., Trial watch: an update of clinical advances in photodynamic therapy and its immunoadjuvant properties for cancer treatment, OncoImmunology 12 (1) (2023) 2226535, http://dx.doi.org/10.1080/2162402X.2023.2226535.

[18] D. Aebisher, S. Czech, K. Dynarowicz, M. Misiołek, K. Komosińska-Vassev, A. Kawczyk-Krupka, D. Bartusik-Aebisher, Photodynamic therapy: Past, current, and future, Int. J. Mol. Sci. 25 (20) (2024) 11325, http://dx.doi.org/10.3390/ijms252011325.

[19] S. Pratavieira, M.B. Requena, M.D. Stringasci, E.T. Ayala, V.S. Bagnato, The physics of light and sound in the fight against skin cancer, Braz. J. Phys. 52 (4) (2022) http://dx.doi.org/10.1007/s13538-022-01121-8.

[20] K.M. Tewari, I.M. Eggleston, Chemical approaches for the enhancement of 5-aminolevulinic acid-based photodynamic therapy and photodiagnosis, Photochem. Photobiol. Sci. 17 (11) (2018) 1553–1572, http://dx.doi.org/10.1039/C8PP00362A.

[21] Y. Zheng, W. Fan, L. Jiang, Y. Lu, Sonophoresis enhances the skin penetration of 5-aminolevulinic acid: A promising pretreatment for photodynamic therapy, Exp. Dermatol. 31 (12) (2022) 1939–1943.

[22] K. Mizutani, D. Watanabe, Y. Akita, M. Akimoto, Y. Tamada, Y. Matsumoto, Photodynamic therapy using direct-current pulsed iontophoresis for 5-aminolevulinic acid application, Photodermatol. Photoimmunol. Photomed. 25 (5) (2009) 280–282.

[23] R.F. Donnelly, D.I. Morrow, P.A. McCarron, A.D. Woolfson, A. Morrissey, P. Juzenas, A. Juzeniene, V. Iani, H.O. McCarthy, J. Moan, Microneedle-mediated intradermal delivery of 5-aminolevulinic acid: Potential for enhanced topical photodynamic therapy, J. Control. Release 129 (3) (2008) 154–162, http://dx.doi.org/10.1016/j.jconrel.2008.05.002, URL https://www.sciencedirect.com/science/article/pii/S0168365908002526.

[24] M.B. Requena, A.D. Permana, J.D. Vollet-Filho, P. González-Vázquez, M.R. Garcia, C.M.G. De Faria, S. Pratavieira, R.F. Donnelly, V.S. Bagnato, Dissolving microneedles containing aminolevulinic acid improves protoporphyrin IX distribution, J. Biophotonics 14 (1) (2021) e202000128, http://dx.doi.org/10.1002/JBIO.202000128.

[25] X. Chen, H. Xiao, Q. Zhao, X. Xu, Y. Cen, D. Xiao, Research hotspot and trend of microneedles in biomedical field: A bibliometric analysis from 2011 to 2020, Burns 48 (4) (2022) 959–972, http://dx.doi.org/10.1016/J.BURNS.2022.04.004.

[26] Z. Sang, T. Zhu, X. Qu, Z. Zhang, W. Wang, Y. Hao, A hyaluronic acid-based dissolving microneedle patch loaded with 5-aminolevulinic acid for improved oral leukoplakia treatment, Colloids Surf. B 245 (2025) 114216, http://dx.doi.org/10.1016/J.COLSURFB.2024.114216.

[27] X. Zhao, X. Li, P. Zhang, J. Du, Y. Wang, Tip-loaded fast-dissolving microneedle patches for photodynamic therapy of subcutaneous tumor, J. Control. Release 286 (2018) 201–209, http://dx.doi.org/10.1016/J.JCONREL.2018.07.038.

[28] Y. Huang, T. Peng, W. Hu, X.Y. Gao, Y. Chen, Q. Zhang, C. Wu, X. Pan, Fully armed photodynamic therapy with spear and shear for topical deep hypertrophic scar treatment, J. Control. Release 343 (2022) 408–419, http://dx.doi.org/10.1016/J.JCONREL.2022.01.043.

[29] Q. Bian, L. Huang, Y. Xu, R. Wang, Y. Gu, A. Yuan, X. Ma, J. Hu, Y. Rao, D. Xu, et al., A facile low-dose photosensitizer-incorporated dissolving microneedles-based composite system for eliciting antitumor immunity and the abscopal effect, Acs Nano 15 (12) (2021) 19468–19479.

[30] J.C. Birchall, Microneedle array technology: the time is right but is the science ready? Expert. Rev. Med. Devices 3 (1) (2006) 1–4.

[31] T. Waghule, G. Singhvi, S.K. Dubey, M.M. Pandey, G. Gupta, M. Singh, K. Dua, Microneedles: A smart approach and increasing potential for transdermal drug delivery system, Biomed. Pharmacother.=Biomedecine Pharmacother. 109 (2019) 1249–1258, http://dx.doi.org/10.1016/J.BIOPHA.2018.10.078.

[32] R.F. Donnelly, D.I. Morrow, M.T. McCrudden, A.Z. Alkilani, E.M. Vicente-Pérez, C. O'Mahony, P. González-Vázquez, P.A. McCarron, A.D. Woolfson, Hydrogel-forming and dissolving microneedles for enhanced delivery of photosensitisers and precursors, Photochem. Photobiol. 90 (3) (2013) 641, http://dx.doi.org/10.1111/PHP.12209.

[33] M. Camović, A. Biščević, I. Brčić, K. Borčak, S. Bušatlić, N. Ćenanović, A. Dedović, A. Mulalić, M. Osmanlić, M. Sirbubalo, A. Tucak, E. Vranić, Coated 3D printed PLA microneedles as transdermal drug delivery systems, IFMBE Proc. 73 (2020) 735–742, http://dx.doi.org/10.1007/978-3-030-17971-7_109.

[34] Y. Gao, M. Hou, R. Yang, L. Zhang, Z. Xu, Y. Kang, P. Xue, PEGDA/PVP microneedles with tailorable matrix constitutions for controllable transdermal drug delivery, Macromol. Mater. Eng. 303 (12) (2018) 1800233, http://dx.doi.org/10.1002/MAME.201800233.

[35] A. Panda, P.K. Sharma, T. McCann, J. Bloomekatz, M.A. Repka, S.N. Murthy, Fabrication and development of controlled release PLGA microneedles for macromolecular delivery using FITC-Dextran as model molecule, J. Drug Deliv. Sci. Technol. 68 (2022) 102712, http://dx.doi.org/10.1016/J.JDDST.2021.102712.

[36] H. Jing, J. Park, B. Kim, Fabrication of a polyglycolic acid porous microneedle array patch using the nonsolvent induced phase separation method for body fluid extraction, Nano Sel. (2024) e202400145, http://dx.doi.org/10.1002/NANO.202400145.

[37] Y.H. Park, S.K. Ha, I. Choi, K.S. Kim, J. Park, N. Choi, B. Kim, J.H. Sung, Fabrication of degradable carboxymethyl cellulose (CMC) microneedle with laser writing and replica molding process for enhancement of transdermal drug delivery, Biotechnol. Bioprocess Eng. 21 (1) (2016) 110–118, http://dx.doi.org/10.1007/S12257-015-0634-7/METRICS.

[38] M. Champeau, Dissolving Microneedles for an Optimal Transdermal Delivery of an Active Principle Used in Photodynamic Therapy: Development and Proof of Concept (Ph.D. thesis), Université de Lille, 2020.

[39] E. Larrañeta, R.E. Lutton, A.D. Woolfson, R.F. Donnelly, Microneedle arrays as transdermal and intradermal drug delivery systems: Materials science, manufacture and commercial development, Mater. Sci. Eng.: R: Rep. 104 (2016) 1–32, http://dx.doi.org/10.1016/J.MSER.2016.03.001.

[40] D.P. Ramirez, L.T. Moriyama, E.R. de Oliveira, N.M. Inada, V.S. Bagnato, C. Kurachi, A.G. Salvio, Single visit PDT for basal cell carcinoma – a new therapeutic protocol, Photodiagnosis Photodyn. Ther. 26 (2019) 375–382, http://dx.doi.org/10.1016/j.pdpdt.2019.04.016, URL https://www.sciencedirect.com/science/article/pii/S1572100019301206.

[41] R.F. Donnelly, L.-W. Ma, P. Juzenas, V. Lani, P.A. McCarron, A.D. Woolfson, J. Moan, Topical bioadhesive patch systems enhance selectivity of protoporphyrin IX accumulation, Photochem. Photobiol. 82 (3) (2006) 670–675, http://dx.doi.org/10.1562/2005-08-08-RA-641, URL https://onlinelibrary.wiley.com/doi/abs/10.1562/2005-08-08-RA-641.

[42] J. Zhu, L. Dong, H. Du, J. Mao, Y. Xie, H. Wang, J. Lan, Y. Lou, Y. Fu, J. Wen, B. Jiang, Y. Li, J. Zhu, J. Tao, 5-aminolevulinic acid-loaded hyaluronic acid dissolving microneedles for effective photodynamic therapy of superficial tumors with enhanced long-term stability, Adv. Heal. Mater. 8 (22) (2019) 1900896, http://dx.doi.org/10.1002/ADHM.201900896.

[43] G. He, Y. Li, M.R. Younis, L.-H. Fu, T. He, S. Lei, J. Lin, P. Huang, Synthetic biology-instructed transdermal microneedle patch for traceable photodynamic therapy, Nat. Commun. 13 (1) (2022) 6238.

[44] C.M. Gardner, N.A. Burke, T. Chu, F. Shen, M.A. Potter, H.D. Stöver, Poly(methyl vinyl ether-alt-maleic acid) polymers for cell encapsulation, J. Biomater. Sci. Polym. Ed. 22 (16) (2011) 2127–2145, http://dx.doi.org/10.1163/092050610X535149.

[45] T. Iglesias, M. Dusinska, N. El Yamani, J.M. Irache, A. Azqueta, A. López de Cerain, In vitro evaluation of the genotoxicity of poly(anhydride) nanoparticles designed for oral drug delivery, Int. J. Pharm. 523 (1) (2017) 418–426, http://dx.doi.org/10.1016/J.IJPHARM.2017.03.016.

[46] C.L. Burnett, W.F. Bergfeld, D.V. Belsito, R.A. Hill, C.D. Klaassen, D.C. Liebler, J.G. MarksJr, R.C. Shank, T.J. Slaga, P.W. Snyder, F.A. Andersen, Final report of the amended safety assessment of PVM/MA copolymer and its related salts and esters as used in cosmetics, Int. J. Toxicol. 30 (5_suppl) (2011) 128S–144S, http://dx.doi.org/10.1177/1091581811407934, PMID: 22068629.

[47] R.F. Donnelly, P.A. McCarron, J.M. Lightowler, A.D. Woolfson, Bioadhesive patch-based delivery of 5-aminolevulinic acid to the nail for photodynamic therapy of onychomycosis, J. Control. Release 103 (2) (2005) 381–392, http://dx.doi.org/10.1016/j.jconrel.2004.12.005, URL https://www.sciencedirect.com/science/article/pii/S016836590400611X.

[48] Y. Li, X. Hu, Z. Dong, Y. Chen, W. Zhao, Y. Wang, L. Zhang, M. Chen, C. Wu, Q. Wang, Dissolving microneedle arrays with optimized needle geometry for transcutaneous immunization, Eur. J. Pharm. Sci. 151 (2020) 105361, http://dx.doi.org/10.1016/j.ejps.2020.105361.

[49] Y.A. Gomaa, D.I.J. Morrow, M.J. Garland, R.F. Donnelly, L.K. El-Khordagui, V.M. Meidan, Effects of microneedle length, density, insertion time and multiple applications on human skin barrier function: assessments by transepidermal water loss, Toxicol. Vitr. 24 (7) (2010) 1971–1978, http://dx.doi.org/10.1016/j.tiv.2010.08.012.

[50] A.S. Cordeiro, I.A. Tekko, M.H. Jomaa, L. Vora, E. McAlister, F. Volpe-Zanutto, M. Nethery, P.T. Baine, N. Mitchell, D.W. McNeill, R.F. Donnelly, Two-photon polymerisation 3D printing of microneedle array templates with versatile designs: Application in the development of polymeric drug delivery systems, Pharm. Res. 37 (9) (2020) 174, http://dx.doi.org/10.1007/s11095-020-02887-9.

[51] G. Anbazhagan, S. Balakrishnapillai Suseela, R. Sankararajan, Design, analysis and fabrication of solid polymer microneedle patch using CO_2 laser and polymer molding, Drug Deliv. Transl. Res. 13 (6) (2023) 1813–1827, http://dx.doi.org/10.1007/s13346-023-01296-w.

[52] H.S. Min, Y. Kim, J. Nam, H. Ahn, M. Kim, G. Kang, M. Jang, H. Yang, H. Jung, Shape of dissolving microneedles determines skin penetration ability and efficacy of drug delivery, Biomater. Adv. 145 (2023) 213248, http://dx.doi.org/10.1016/j.bioadv.2022.213248.

[53] M.J. Borja, Gantrez hydrogel with dry tack, 2013, US20130195771A1. URL https://patents.google.com/patent/US20130195771A1/en.

[54] K. Migalska, D.I.J. Morrow, M.J. Garland, R. Thakur, A.D. Woolfson, R.F. Donnelly, Laser-engineered dissolving microneedle arrays for transdermal macromolecular drug delivery, Pharm. Res. 28 (8) (2011) 1919–1930, http://dx.doi.org/10.1007/s11095-011-0419-4.

[55] A.K.L. Fujita, P.G.S. Rodrigues, M.B. Requena, A. Escobar, R.W. da Rocha, A.B.d. Nardi, C. Kurachi, P.F.C. de Menezes, V.S. Bagnato, Fluorescence evaluations for porphyrin formation during topical PDT using ALA and methyl-ALA mixtures in pig skin models, Photodiagnosis Photodyn. Ther. 15 (2016) 236–244, http://dx.doi.org/10.1016/J.PDPDT.2016.05.008.

[56] O. Olatunji, D.B. Das, M.J. Garland, L. Belaid, R.F. Donnelly, Influence of array interspacing on the force required for successful microneedle skin penetration: theoretical and practical approaches, J. Pharm. Sci. 102 (4) (2013) 1209–1221, http://dx.doi.org/10.1002/jps.23439.

[57] E. Larrañeta, J. Moore, E.M. Vicente-Pérez, P. González-Vázquez, R. Lutton, A.D. Woolfson, R.F. Donnelly, A proposed model membrane and test method for microneedle insertion studies, Int. J. Pharm. 472 (1–2) (2014) 65–73.

[58] A.D. Permana, M. Mir, E. Utomo, R.F. Donnelly, Bacterially sensitive nanoparticle-based dissolving microneedles of doxycycline for enhanced treatment of bacterial biofilm skin infection: A proof of concept study, Int. J. Pharm.: X 2 (2020) 100047, http://dx.doi.org/10.1016/S2590156720300098.

[59] M.B. Requena, T.Q. Corrêa, D.L. Sara Bejar, J.C. Barreiro, K.T. de Paula, V.S. Bagnato, C.B. Michelle Requena, S. Carlos, Ozone as a method for decontamination of dissolving microneedles for clinical use, Photochem. Photobiol. 00 (2025) 1–10.

[60] Y.J. Lim, S.R. Jeon, J.M. Koh, H.G. Wu, Tumor growth suppression and enhanced radioresponse by an exogenous epidermal growth factor in mouse xenograft models with A431 cells, Cancer Res. Treat. : Off. J. Korean Cancer Assoc. 47 (4) (2015) 921–930, http://dx.doi.org/10.4143/CRT.2014.153.

[61] M. Di Benedetto, A. Starzec, R. Vassy, G.Y. Perret, M. Crépin, M. Kraemer, Inhibition of epidermoid carcinoma A431 cell growth and angiogenesis in nude mice by early and late treatment with a novel dextran derivative, Br. J. Cancer 88 (12) (2003) 1987–1994, http://dx.doi.org/10.1038/SJ.BJC.6600985.

[62] M.R. Garcia, M.B. Requena, S. Pratavieira, L.T. Moriyama, M. Becker, V.S. Bagnato, C. Kurachi, D.V. Magalhães, Development of a system to treat and online monitor photodynamic therapy of skin cancer using PpIX near-infrared fluorescence, Photodiagnosis Photodyn. Ther. 30 (2020) 101680, http://dx.doi.org/10.1016/J.PDPDT.2020.101680.

[63] S. Mordon, Painless and efficient ALA-PDT and MAL-PDT of actinic keratosis can be achieved by drastically reducing the drug-light interval, Dermatol. Ther. 33 (3) (2020) e13423, http://dx.doi.org/10.1111/DTH.13423.

[64] H. Wang, J. Li, T. Lv, Q. Tu, Z. Huang, X. Wang, Therapeutic and immune effects of 5-aminolevulinic acid photodynamic therapy on UVB-induced squamous cell carcinomas in hairless mice, Exp. Dermatol. 22 (5) (2013) 362–363, http://dx.doi.org/10.1111/EXD.12132.

[65] P.G.S. Rodrigues, P.F.C. de Menezes, A.K.L. Fujita, A. Escobar, A.B. de Nardi, C. Kurachi, V.S. Bagnato, Assessment of ALA-induced PpIX production in porcine skin pretreated with microneedles, J. Biophotonics 8 (9) (2015) 723–729, http://dx.doi.org/10.1002/JBIO.201400081.

[66] C. Grecco, H. Buzzá, M. Stringasci, J. Andrade, S. Pratavieira, A. Zanchin, A. Tuboy, V. Bagnato, Single LED-based device to perform widefield fluorescence imaging and photodynamic therapy, Biophotonics South Am. 9531 (2015) 953121, http://dx.doi.org/10.1117/12.2185925.

[67] M.R. Garcia, S. Pratavieira, L.T. Moriyama, C. Kurachi, D.V. Magalhães, Assembly of a PDT device with a near-infrared fluorescence monitoring of PpIX during treatment, in: Optical Methods for Tumor Treatment and Detection: Mechanisms and Techniques in Photodynamic Therapy XXVIII, vol. 10860, SPIE, 2019, pp. 82–88.

[68] C. de Paula Campos, C. de Paula D'Almeida, M.S. Nogueira, L.T. Moriyama, S. Pratavieira, C. Kurachi, Fluorescence spectroscopy in the visible range for the assessment of UVB radiation effects in hairless mice skin, Photodiagnosis Photodyn. Ther. 20 (2017) 21–27, http://dx.doi.org/10.1016/j.pdpdt.2017.08.016, URL https://www.sciencedirect.com/science/article/pii/S1572100017302806.

[69] E.T.P. Ayala, M.B. Requena, V.S. Bagnato, S. Pratavieira, Quantification of protoporphyrin IX in murine pigmented melanoma induced by systemic and topical ALA administration protocols, in: Optical Methods for Tumor Treatment and Detection: Mechanisms and Techniques in Photodynamic Therapy XXXII, vol. 12823, SPIE, 2024, pp. 55–62, http://dx.doi.org/10.1117/12.3005054.

[70] X. Hong, L. Wei, F. Wu, Z. Wu, L. Chen, Z. Liu, W. Yuan, Dissolving and biodegradable microneedle technologies for transdermal sustained delivery of drug and vaccine, DDDT 7 (2013) 945–952, http://dx.doi.org/10.2147/DDDT.S44401.

[71] P.A. McCarron, R.F. Donnelly, G.P. Andrews, A.D. Woolfson, Stability of 5-aminolevulinic acid in novel non-aqueous gel and patch-type systems intended for topical application, J. Pharm. Sci. 94 (8) (2005) 1756–1771, http://dx.doi.org/10.1002/JPS.20393.

[72] V. Chimisso, M.A. Aleman Garcia, S. Yorulmaz Avsar, I.A. Dinu, C.G. Palivan, Design of bio-conjugated hydrogels for regenerative medicine applications: From polymer scaffold to biomolecule choice, Molecules 25 (18) (2020) http://dx.doi.org/10.3390/molecules25184090, URL https://www.mdpi.com/1420-3049/25/18/4090.

[73] R.F. Donnelly, T.R.R. Singh, M.J. Garland, K. Migalska, R. Majithiya, C.M. McCrudden, P.L. Kole, T.M.T. Mahmood, H.O. McCarthy, A.D. Woolfson, Hydrogel-forming microneedle arrays for enhanced transdermal drug delivery, Adv. Funct. Mater. 22 (23) (2012) 4879–4890, http://dx.doi.org/10.1002/ADFM.201200864.

[74] I.A. de Lima, L.G. Fiuza, J.S.D. Tovar, D.S.L. Bejar, A.J.B. Tomé, M.B. Requena, L. Pires, G. Zheng, N.M. Inada, C. Kurachi, V.S. Bagnato, Strategies for overcoming the lung surfactant barrier and achieving success in antimicrobial photodynamic therapy, J. Photochem. Photobiol. 24 (2024) 100252, http://dx.doi.org/10.1016/J.JPAP.2024.100252.

[75] M.T. McCrudden, A.Z. Alkilani, C.M. McCrudden, E. McAlister, H.O. McCarthy, A.D. Woolfson, R.F. Donnelly, Design and physicochemical characterisation of novel dissolving polymeric microneedle arrays for transdermal delivery of high dose, low molecular weight drugs, J. Control. Release 180 (2014) 71–80.

[76] A. Iyer, V.G. Jyothi, A. Agrawal, D.K. Khatri, S. Srivastava, S.B. Singh, J. Madan, Does skin permeation kinetics influence efficacy of topical dermal drug delivery system?: Assessment, prediction, utilization, and integration of chitosan biomacromolecule for augmenting topical dermal drug delivery in skin, J. Adv. Pharm. Technol. Res. 12 (4) (2021) 345, http://dx.doi.org/10.4103/JAPTR.JAPTR_82_21.

[77] M.T. Pires, A.D. Pereira, S.M. Durães, M.C. Issa, M. Pires, Laser-assisted MAL-PDT associated with acoustic pressure wave ultrasound with short incubation time for field cancerization treatment: A left-right comparison, Photodiagnosis Photodyn. Ther. 28 (2019) 216–220, http://dx.doi.org/10.1016/J.PDPDT.2019.08.034.

[78] M. Champeau, D. Jary, L. Mortier, S. Mordon, S. Vignoud, A facile fabrication of dissolving microneedles containing 5-aminolevulinic acid, Int. J. Pharm. 586 (2020) 119554.

[79] E. Christensen, C. Mørk, O.A. Foss, Pre-treatment deep curettage can significantly reduce tumour thickness in thick basal cell carcinoma while maintaining a favourable cosmetic outcome when used in combination with topical photodynamic therapy, J. Ski. Cancer 2011 (2011) 1–6, http://dx.doi.org/10.1155/2011/240340.

[80] L.E. Heusinkveld, T.A. Bullock, J. Negrey, C.B. Warren, E.V. Maytin, Sandpaper curettage: A simple method to improve PDT outcomes for actinic keratosis, Photodiagnosis Photodyn. Ther. 40 (2022) 103050.

[81] P. Palasuberniam, D. Kraus, M. Mansi, A. Braun, R. Howley, K.A. Myers, B. Chen, Ferrochelatase deficiency abrogated the enhancement of aminolevulinic acid-mediated protoporphyrin IX by iron chelator deferoxamine, Photochem. Photobiol. 95 (4) (2019) 1052, http://dx.doi.org/10.1111/PHP.13091.

[82] K. Berg, H. Anholt, J. Moan, The influence of iron chelators on the accumulation of protoporphyrin IX in 5-aminolaevulinic acid-treated cells, Br. J. Cancer 74 (1996).

[83] Y.C. Kim, J.H. Park, M.R. Prausnitz, Microneedles for drug and vaccine delivery, Adv. Drug Deliv. Rev. 64 (14) (2012) 1547–1568, http://dx.doi.org/10.1016/J.ADDR.2012.04.005.

[84] R.F. Donnelly, D.I. Morrow, P.A. McCarron, P. Juzenas, A.D. Woolfson, Pharmaceutical analysis of 5-aminolevulinic acid in solution and in tissues, J. Photochem. Photobiol. B: Biol. 82 (1) (2006) 59–71, http://dx.doi.org/10.1016/J.JPHOTOBIOL.2005.08.007.

[85] R.F. Donnelly, P.A. McCarron, A.D. Woolfson, Derivatives of 5-aminolevulinic acid for photodynamic therapy, Perspect. Med. Chem. 1 (2007) 49, http://dx.doi.org/10.1177/1177391x0700100005.

[86] E.T.P. Ayala, I.S.e. Carvalho, C.A. Antunes, A. Mahmood, M.B. Requena, F. Alves, L. Pires, V. Yakovlev, V.S. Bagnato, S. Pratavieira, Comparative analysis of ALA mediated sonodynamic therapy considering tumor size, light combination and ultrasound delivery in murine cutaneous melanoma, Sci. Rep. 15 (1) (2025) 30859.

[87] M.D. Stringasci, J.D.V. Filho, L.T. Moriyama, C. Kurachi, V.S. Bagnato, Investigation of protoporphyrin IX production induced by aminolevulinic acid combined with thermogenic and/or vasodilator substances, in: T. Hasan (Ed.), in: 17th International Photodynamic Association World Congress, vol. 11070, SPIE, International Society for Optics and Photonics, 2019, p. 110706Q, http://dx.doi.org/10.1117/12.2525696.

[88] H. Kathuria, D. Lim, J. Cai, B.G. Chung, L. Kang, Microneedles with tunable dissolution rate, ACS Biomater. Sci. Eng. 6 (9) (2020) 5061–5068.

[89] R.F. Donnelly, Clinical translation and industrial development of microneedle-based products, in: R.F. Donnelly, T.R. Singh (Eds.), Microneedles for Drug and Vaccine Delivery and Patient Monitoring, John Wiley & Sons, Ltd., 2018, pp. 307–322, http://dx.doi.org/10.1002/9781119305101.ch11.

[90] B. Creelman, C. Frivold, S. Jessup, G. Saxon, C. Jarrahian, Manufacturing readiness assessment for evaluation of the microneedle array patch industry: an exploration of barriers to full-scale manufacturing, Drug Deliv. Transl. Res. 12 (2) (2022) 368–375, http://dx.doi.org/10.1007/s13346-021-01076-4.